MATERIALS SCIENCE

Concentric ice-templating of ultracompressible tough hydrogels with bioinspired circumferentially aligned architecture

Wenxi Gu[1,2], Shuqi Yang[1,2], Dazhe Zhao[1,2], Yiwei Zou[1,2], Chonghao Chen[3], Peiqi Niu[1,2], Xiangyu Liang[4], Chi Tat Kwok[1], Bingpu Zhou[5], Chunming Wang[3], Yan Yan Shery Huang[6], Ji Liu[7], Iek Man Lei[1,2]*

Materials with circumferentially aligned fibers, such as intervertebral discs and arteries, are abundant in nature but challenging to replicate artificially, despite their mechanical advantages. Although ice-templating can create bioinspired materials, the achievable structures remain limited to simple forms, such as honeycomb, lamellar, and radial structures. Here, we developed a unique ice-templating technique that constructs circumferential fibrous structures in hydrogels through slow freezing. Enhanced with rotary compression annealing, these hydrogels exhibit record-breaking features that cannot concurrently be achieved in conventional ice-templated and top-performing tough hydrogels, including high tensile properties, isotropic fatigue threshold of 2320 joules per square meter, ultracompressibility (8% strain after 500 cycles), and extraordinary burst pressure of 1.6 bar while maintaining 85 weight % water content. These properties enable opportunities in robotics, including hydrogel pneumatic grippers and an untethered bioinspired robotic fish that exhibits high-force actuation and long-term robustness. Our approach enriches the diversity of bioinspired structures in artificial materials, establishing exceptional mechanical properties through cross-length scale structural design.

INTRODUCTION

Nature has an impressive ability to create materials with fascinating combinations of properties from a limited palette of ingredients (*1*, *2*), showcasing the importance of architecture in determining their mechanical (*1*, *3*), optical (*4*), thermal (*5*), and many other properties. This astonishing capability has long inspired material scientists to develop synthetic materials that match or even surpass the performance of their natural counterparts, particularly in the field of hydrogel mechanics (*6*). As conventional hydrogels are typically brittle due to their single and amorphous polymer networks (*7*), harnessing biomimetic structural designs to promote their mechanical performance is highly desirable. Such materials can unlock unprecedented opportunities in tissue engineering, flexible devices, robotics, and other cutting-edge applications (*8*, *9*).

Ice-templating, or freeze-casting, is a simple approach for fabricating hydrogels with bioinspired structures by controlling directional ice growth within a polymeric solution (*10*, *11*). Although this technique can impart extreme mechanical properties to hydrogels, such as tissue-like toughness (*12*, *13*), fatigue resistance (*14*–*16*), and impact resistance (*17*), the achievable structures through ice-templating remain severely limited. Common achievable structures, including honeycomb (*18*–*20*), lamellar (*21*–*23*), and radial structures (*24*), cannot capture the rich diversity found in nature (*25*). Therefore, new fabrication strategies that can replicate the different unique structural designs present in nature are highly in demand to broaden the range of properties realizable in artificial hydrogels.

Circumferential fibrous structures are commonly found in natural materials, such as intervertebral discs, arteries, and fish swim bladders. These structures are essential for withstanding internal pressure and mechanical loads (*26*–*30*). For example, the concentric rings of intervertebral discs enable load-bearing ability for withstanding millions of movements over a lifetime while having high water content (*31*). The concentric wall structures of arteries with circumferentially aligned collagen fibers can effectively bear the stress caused by physiological pressure from billions of cardiac cycles (*32*, *33*). Although some studies have explored the development of artificial materials with concentric structures, such as the onion-like hydrogels with macroscale concentric features (*34*, *35*) and the concentric ceramics created using freeze-casting with an external acoustic field (*36*), creating hydrogels with circumferentially fibrous structure at microscale using ice-templating has not reported until now. This is likely due to the difficulties in controlling ice development in hydrogels in a circumferential manner.

Here, we report the successful use of ice-templating to create bioinspired hydrogels with concentrically aligned fibrous structures (Fig. 1, A and B). This was achieved by controlling columnar ice growth parallel to the cold wall of a cylindrical mold within a polymeric solution under slow freezing. By synergistically combining this approach with a rotary compression annealing technique, the resulting concentric fibrous hydrogels exhibit a record-breaking combination of mechanical properties, including a high tensile strength of 14 MPa, an average tensile toughness of 21 MJ/m^3, an isotropic fatigue threshold of 2320 J/m^2, extraordinary compressibility with a residual strain of 8% after 500 cyclic loadings at 60% strain, and a remarkable pressure-withstanding capability with a burst pressure of 1.6 bar (Fig. 1C). Such combined properties cannot

[1]Department of Electromechanical Engineering, University of Macau, Macau 999078, China. [2]Centre for Artificial Intelligence and Robotics, University of Macau, Macau 999078, China. [3]State Key Laboratory of Quality Research in Chinese Medicine, Institute of Chinese Medical Sciences, University of Macau, Macau 999078, China. [4]Agricultural Genomics Institute at Shenzhen, Chinese Academy of Agricultural Sciences, Shenzhen 518000, China. [5]Joint Key Laboratory of the Ministry of Education, Institute of Applied Physics and Materials Engineering, University of Macau, Macau 999078, China. [6]Department of Engineering, University of Cambridge, Cambridge CB2 1PZ, UK. [7]Department of Mechanical and Energy Engineering, Southern University of Science and Technology, Shenzhen 518055, China.
*Corresponding author. Email: ieklei@um.edu.mo

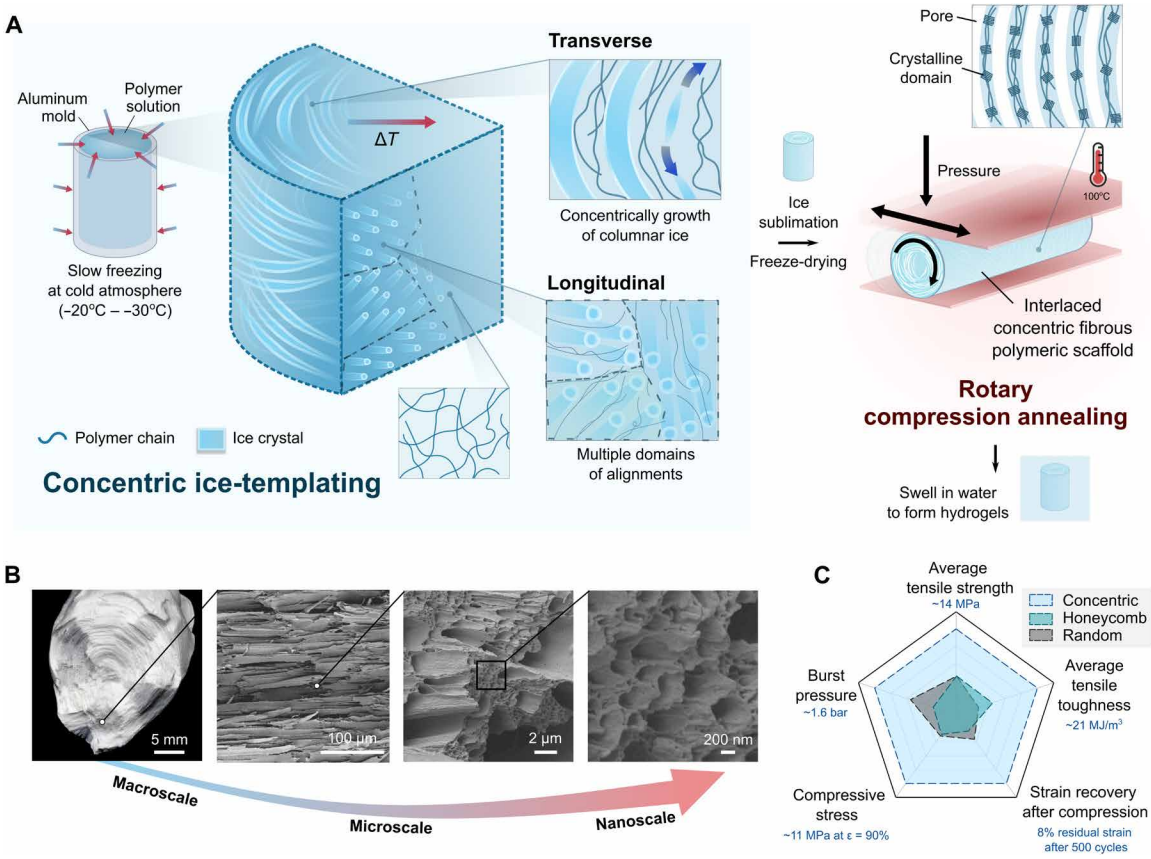

Fig. 1. Fabrication of hydrogels with interlaced concentric fibrous structures. (**A**) Schematic illustration depicting a synergistic approach that combines concentric ice-templating under slow freezing with rotary compression annealing to result in concentric fibrous hydrogels (concentric-RA) with substantially enhanced mechanical properties. (**B**) Photograph and SEM images displaying the hierarchical structure of the polymeric scaffold created using concentric ice-templating, ranging from macrostructures to nanostructures. (**C**) Radar plot comparing the mechanical performance metrics of the concentric fibrous hydrogels to hydrogels with honeycomb and random structures. The data used to evaluate the performance metrics are summarized in table S1, and the blue texts indicate the performance with the concentric fibrous hydrogels treated by 3 hours of rotary compression annealing. ε, strain.

be achieved in hydrogels with honeycomb or random structures, opening up a wide range of potential applications, including high-force pneumatic hydrogel actuators capable of withstanding high internal pressures, mimicking the biomechanical functionality of fish swim bladder, as well as an untethered bioinspired robotic swimming fish with hydrogel actuators functioning as bionic muscles with robustness over 80,000 actuation cycles. Our concentric ice-templating technique represents an important paradigm for manufacturing biomimetic structural materials, enriching the design possibilities through ice-templating.

RESULTS

Concentric ice-templating

Figure 1A and fig. S1 illustrate our fabrication strategy to create hydrogels with bioinspired interlaced concentric fibrous structures. In this study, poly(vinyl alcohol) (PVA) with a 99% hydrolysis degree was used due to its prevalent use in hydrogel mechanics and freeze-casting research. Typically, a 5% (w/v) PVA solution was injected into a custom-made thin-walled cylindrical mold, followed by slow freezing in a controlled −30°C atmosphere (freezing rate = −2.1°C/min). The ice was subsequently sublimated via freeze-drying. Unlike conventional freeze-casting techniques that typically produce lamellar, honeycomb, or radial structures, our method uniquely produces three-dimensional (3D) polymeric scaffolds with interlaced concentric fibrous structures. Micro-computed tomography (μ-CT) scan and scanning electron microscopy (SEM) confirm that the transverse cross section of these scaffolds exhibits a concentrically aligned fibrous structure, with the concentric feature converging at the center (Fig. 2, A and B). The longitudinal cross section displays a multidomain aligned structure, forming an interlaced structural network (Fig. 2D and fig. S2). Movie S1 illustrates the 3D structure of the scaffold reconstructed from the μ-CT scan, confirming the interlaced concentric fibrous architecture. The concentric fibrous structure can be retained in the hydrogel after reswelling, as evidenced by confocal microscopy images (Fig. 2C). Such concentric architectures in hydrogels have not been achieved with existing ice-templating methods.

To understand the formation of the concentric fibrous structures in polymer solutions, we observed the freezing process in situ. Movie S2 illustrates the freezing mechanism for achieving concentric fibrous polymeric scaffolds proposed based on our observation. Our observation reveals that freezing rate is pivotal in determining the structure. When the polymeric solution is directionally frozen

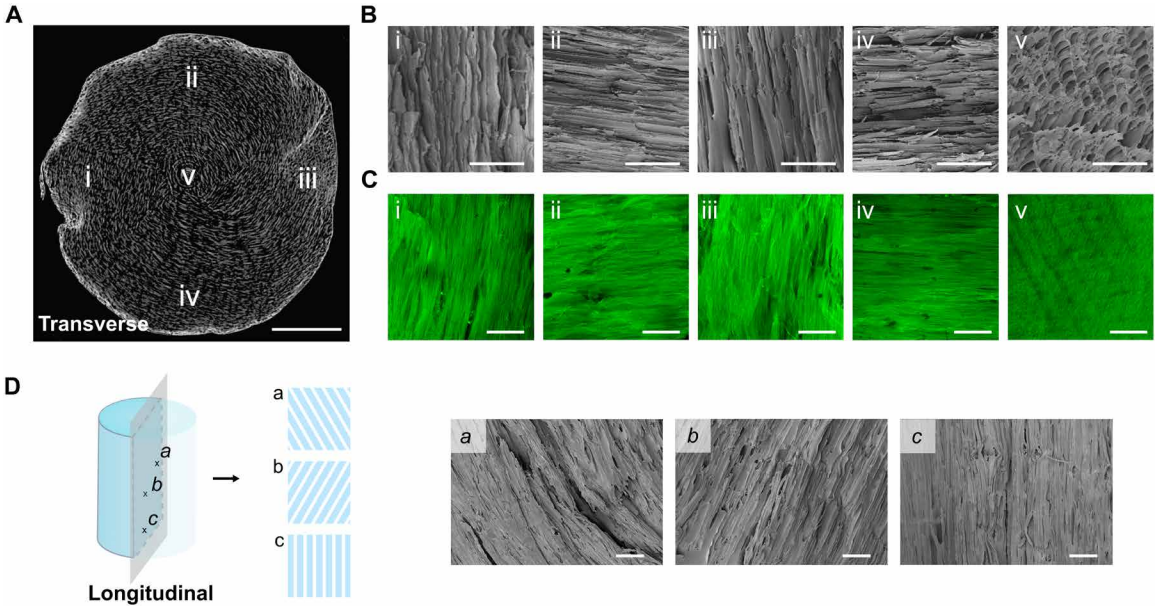

Fig. 2. Structural characterizations. (**A**) μ-CT image showing the transverse section of the polymeric scaffold produced by concentric ice-templating exhibiting a characteristic concentric structure. Scale bar, 1 mm. (**B**) Representative SEM images taken from the transverse cross section displaying the concentric fibrous structure. Scale bars, 100 μm. (**C**) Confocal images depicting that the concentric fibrous structure can be preserved after reswelling the polymeric scaffold in water to form hydrogels. Scale bars, 100 μm. The directionality assessments of the structures showed in (B) and (C) can be found in fig. S3. (**D**) SEM images captured at three random locations in the longitudinal cross section, revealing the multidomain alignments of polymer fibers. Scale bars, 100 μm. All samples were prepared from a 5% (w/v) PVA solution freezing at a −30°C atmosphere.

slowly at −20°C (freezing rate = ~−1.5°C/min), ice preferentially nucleates near the cold surface and forms columnar ice that grows parallel to the cold surface (Fig. 3A and movie S3). Meanwhile, the ice nucleates successively toward the warmer region from the cold surface. In contrast, fast freezing at −50°C (freezing rate = ~−3.8°C/min) leads to the formation of dendritic ice crystals that grow rapidly along the temperature gradient and perpendicular to the cooling surface (Fig. 3B and movie S3). Therefore, by slowly freezing the polymeric solution in a cylindrical mold, columnar ice can be developed circumferentially within the polymer solution (Fig. 3C). This process slowly expels the polymer chains toward the ice boundaries, yielding concentric fibrous scaffolds. Figure 3D and fig. S4 confirm the structures of the polymeric scaffolds fabricated with different freezing temperatures. Slow freezing conditions (i.e., in a −20° to −40°C atmosphere with a rate of −1.5° to −2.9°C/min) resulted in scaffolds displaying a concentric morphology at their transverse cross section. On the other hand, radially aligned scaffolds were formed under fast freezing conditions (freezing at <−50°C, a freezing rate faster than −3.8°C/min), corroborating the findings of previous works (*24*, *37*, *38*).

Compared with conventional freeze-thawing, which also involves slow freezing at a relatively high freezing temperature (*39*), our method uses a one-time freezing process to produce concentric fibrous polymeric scaffolds. When repeating the freeze-thaw cycles, the concentric structure transitioned to a random porous structure, similar to those reported in previous freeze-thawed hydrogels (*40*) (fig. S5). This is due to microstructural distortion during the repeated freezing and thawing processes. Using concentric ice-templating, the polymeric scaffolds predominantly display a concentric structure at different transverse planes along the longitudinal axis (fig. S6). The concentric structure can be readily found at planes less than 1 cm away from both the top and bottom sides of the sample. Such uniformity likely results from preferential ice nucleation at the concave surface rather than the flat bottom and top surfaces (*41*). In addition, the multiple domain alignments observed in the longitudinal cross section, shown in the SEM images and μ-CT scan, indicate that the concentric ices grew in a nonplanar manner, leading to an interlaced concentric fibrous structure (figs. S2 and S7 and movie S1). It is important to note that such concentric fibrous structures cannot be attained using conventional bottom-up freeze-casting with liquid nitrogen and a 3D spiral insulating substrate, attributed to the difficulties in generating a circumferential temperature gradient in the polymeric solution with this method (see Supplementary Text S1).

Customizability and scalability

Concentric ice-templating not only eliminates the need for expensive cryogenic agents and laborious monitoring required in conventional freeze-casting but also allows the creation of structural hydrogels using a standard freezer, enhancing scalability and convenience. We confirmed that concentric fibrous polymeric scaffolds can similarly be attained using a standard freezer (fig. S9). Furthermore, scaffolds of varying diameters (e.g., 5 to 18 mm) and lengths (e.g., 2 to 16 cm) can be readily fabricated in a customizable and mass-producible manner with consistent alignment and similar compartment size spacing of ~10 μm along their entire longitudinal axis (Fig. 3E and figs. S10 to S12). Although slight variations in compartment size were observed in the transverse cross section attributed to the differing low temperature at the migrating ice front, this can potentially be addressed using the recently reported additive freeze-casting method (*42*) (fig. S13). Concentric ice-templating is also extendable to any arbitrary molds for constructing microstructural alignments conforming to their

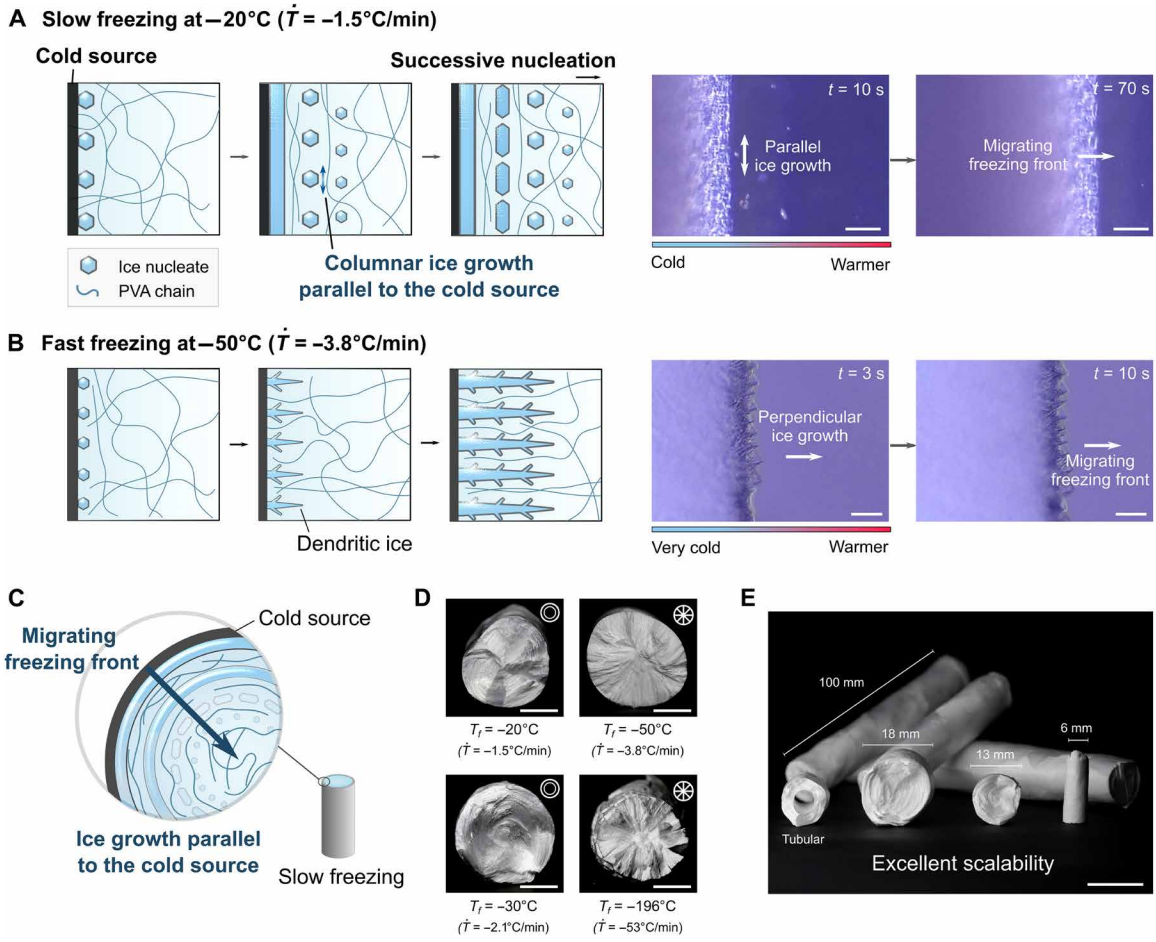

Fig. 3. Freezing mechanism and scalable technique. (**A** and **B**) Schematic illustration and top-view optical images depicting the freezing processes conducted under slow freezing at −20°C (A) and fast freezing at −50°C (B). The results indicate that columnar ice growth occurred parallel to the cold source under slow freezing, whereas dendritic ice grew perpendicular to the cold source during fast freezing. Scale bars, 100 μm. Video of the freezing processes can be found in movie S3. (**C**) Schematic diagram of the freezing mechanism for developing concentrically templated ice in polymeric solutions using a cylindrical container. (**D**) Photographs showing the transverse cross sections of polymeric scaffolds with different structures prepared using different freezing temperatures. Scale bars, 5 mm. T_f and $\dot{T}$ refer to the temperature of the freezing chamber and the corresponding freezing rate, respectively. (**E**) Photographs of the polymeric scaffolds with a variety of dimensions and shapes exhibiting similar concentric structures, fabricated using concentric ice-templating. Scale bar, 15 mm.

outer boundaries, such as rectangular and vessel-like tubular constructs (fig. S14). In addition, we also proved that this technique is applicable to other polymeric systems. Similar concentric fibrous structures can be produced with silk and chitosan–graphene oxide solutions at a slow freezing temperature of −30°C (fig. S15, A and B; see Supplementary Text S2 for discussion).

Mechanical toughening via rotary compression annealing

Next, we designed a rotary compression annealing strategy that can effectively toughen the concentric fibrous hydrogels (Fig. 1A and fig. S16A). Differing from conventional compression annealing that is limited to film-like materials, our rotary compression annealing method involves mechanical pressure being gradually applied to a rotating and dried sample at 100°C. This process can preserve the characteristic concentric structure while promoting the rearrangement of polymer chains to induce nanocrystalline domains and increasing the internal friction between polymer chains. As shown in Fig. 4A and fig. S16B, a highly densified concentric fibrous structure was resulted after a 3-hour rotary compression annealing treatment.

To elucidate the effect of our fabrication approach on crystallinity, we prepared samples for comparison, including freeze-thawed five-cycle PVA with annealing (random-A), honeycomb PVA produced by unidirectional freeze-casting and annealing (honeycomb-A), and concentric fibrous PVA treated by annealing (concentric-A) and rotary compression annealing for different durations (concentric-RA). Figure 4B illustrates the structures of concentric fibrous, honeycomb, and random hydrogels. Differential scanning calorimetry (DSC) measurements reveal that the crystallinities of the concentric-A and honeycomb-A samples are similar, suggesting that concentric ice-templating is capable of forming high-density crystalline domains similar to conventional freeze-casting (Fig. 4C and fig. S18). Longer rotary compression annealing remarkably enhanced crystallinity, which reached 30.0 wt % (at its dry state) after 5 hours, surpassing all the polymeric scaffolds tested here. After reswelling, all concentric-RA hydrogels still retained over 82 wt % water content (Fig. 4C).

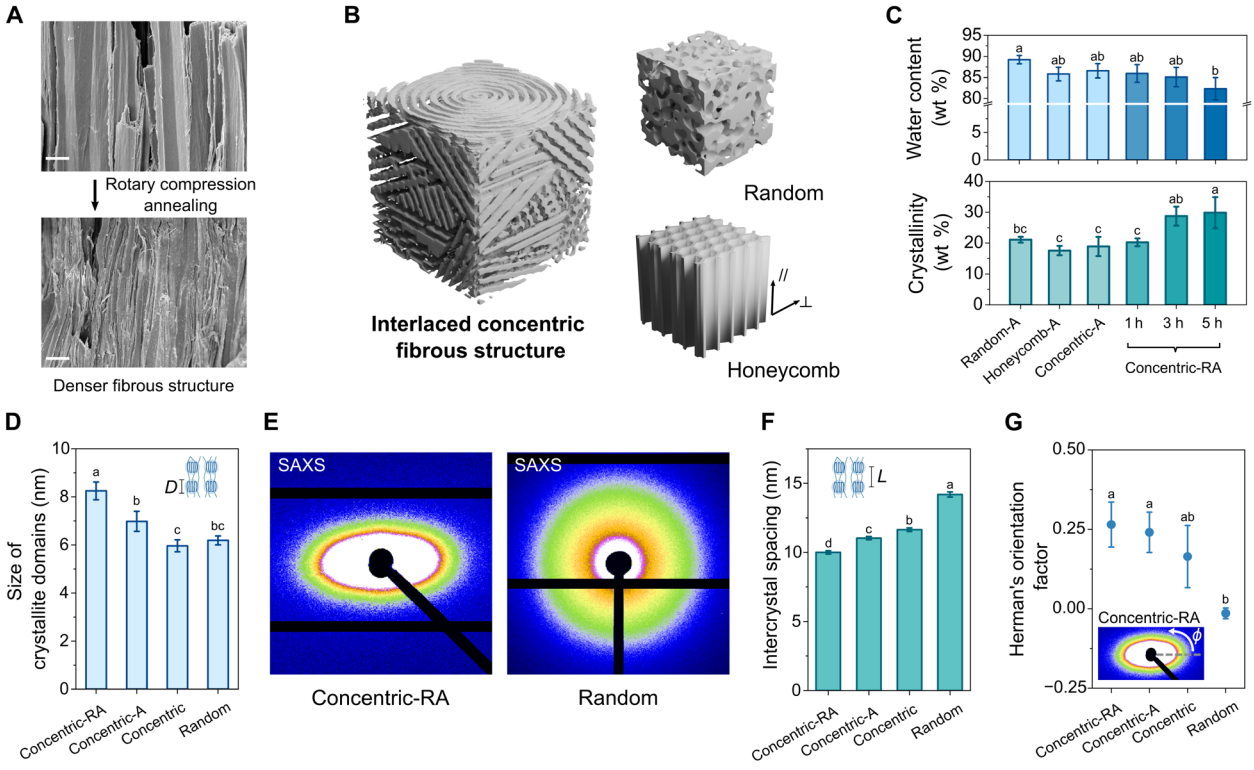

Fig. 4. Crystallinity and crystalline structures. (**A**) SEM images showing the microstructure of the polymeric scaffolds before and after rotary compression annealing for 3 hours. Scale bars, 10 μm. (**B**) Schematic illustrations depicting the morphologies of hydrogels with concentric fibrous, honeycomb, and random structures. (**C**) Summary of crystallinities and water contents of random-A, honeycomb-A, concentric-A, and concentric-RA hydrogels treated with rotary compression annealing times of 1, 3, and 5 hours (h). All annealed (-A) samples were treated with 90 min of annealing. (**D**) Average size of the crystalline domains (*D*) of different hydrogels determined from WAXS. (**E**) 2D SAXS patterns of concentric-RA and random hydrogels. (**F**) Average intercrystal spacing (*L*) determined by SAXS. (**G**) Calculated Herman's orientation factors. Data in [(C), (D), (F), and (G)] are means ± SD, $n = 3$ independent samples. Different letters in [(C), (D), (F), and (G)] indicate statistically significant differences between groups ($P < 0.05$), determined using one-way ANOVA with Tukey's test.

To investigate the crystalline morphology and nanostructures of the hydrogels, we carried out wide-angle x-ray scattering (WAXS) and small-angle x-ray scattering (SAXS) measurements. The 1D WAXS patterns reveal that all hydrogels, including the concentric-RA, concentric-A, concentric, and random hydrogels, exhibit diffraction peaks at $2\theta = \sim 15.6°$ (corresponding to a *d*-spacing of ~4.56 Å, calculated using Bragg's law) (fig. S19B). These peaks are associated with the $(10\bar{1})$ reflection of PVA (*43*, *44*), confirming their crystalline nature. Notably, the sharper peak for the concentric-RA hydrogel suggests a significantly increased crystalline domain size (*D*) of 8.2 nm, as determined using the Scherrer equation (Fig. 4D). This finding supports the effectiveness of rotary compression annealing in increasing crystallinity compared to conventional annealing. Furthermore, SAXS measurements were used to analyze the intercrystal spacing (*L*) of the hydrogels (Fig. 4, E and F, and fig. S20). The Iq^2 versus *q* SAXS intensity profile of the concentric-RA hydrogels exhibits a peak at $q = \sim 0.063$ Å^{-1}, corresponding to an intercrystal spacing (*L*) of ~10.0 nm, estimated by the Bragg expression ($L = 2\pi/q_{max}$) (Fig. 4F and fig. S20A). This intercrystal spacing is smaller than that of the control samples, indicating a more densely packed nanocrystalline structure in the concentric-RA hydrogels (Fig. 4F). In addition, azimuthal angle analyses for the concentric-RA, concentric-A, and concentric hydrogels indicate anisotropic nanostructures (fig. S20B). The calculated Herman's orientation factors for these hydrogels are 0.27, 0.24, and 0.16, respectively, confirming aligned nanofibril orientations (Fig. 4G). In contrast, the Herman's orientation factor of random hydrogels is −0.01, which suggests a highly isotropic structure.

Tensile properties

Having established the method to fabricate concentric fibrous hydrogels with enhanced crystallinity, we then investigated the effect of their structure on mechanical performance. First, we compared their tensile properties with control samples after reswelling them in deionized water till equilibrium. The concentric-RA$_{||}$ hydrogels measured in the longitudinal direction exhibited substantial improvements in tensile modulus and toughness, with increases of ~2.9- and 1.4-fold, respectively, compared to the honeycomb-RA$_{||}$ hydrogels treated with the same rotary compression annealing process (Fig. 5, A and B, and fig. S21B).

Moreover, our concentric fibrous hydrogels can be made into tubular shapes and readily transformed into 2D hydrogel sheets (referred to as conc2sheet hydrogels) that exhibit an isotropic interlaced fibrous structure (Fig. 5C; see fig. S21D for the fabrication). Through the synergy of concentric ice-templating and rotary compression annealing, the conc2sheet-RA hydrogels demonstrated outstanding isotropic mechanical performance, including a 2.2-fold increase in tensile modulus compared to the honey2sheet-RA$_{||}$ hydrogels, as

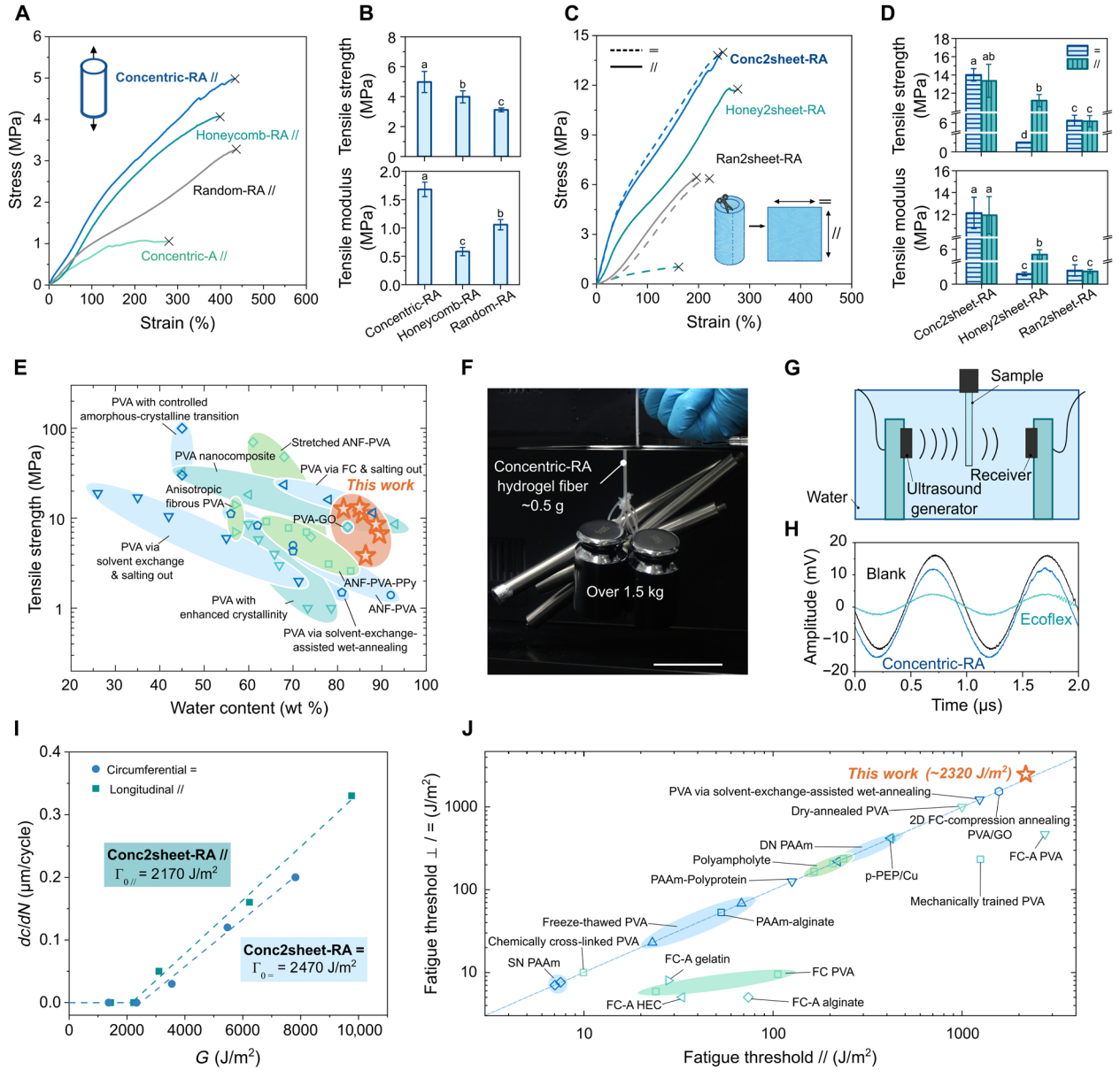

Fig. 5. Tensile properties and fatigue threshold. (**A**) Representative tensile stress-strain curves comparing concentric-RA hydrogels with other hydrogels in the longitudinal (//) direction. (**B**) Summary of the tensile strengths and moduli of different hydrogels treated with rotary compression annealing. (**C**) Representative tensile stress-strain curves comparing conc2sheet-RA hydrogels with other hydrogels in both longitudinal (//) and circumferential (=) directions. The inset schematic shows that concentric-RA hydrogels with tubular shapes can be cut to form hydrogel sheets (conc2sheet-RA) that exhibit an interlaced fibrous structure and isotropic mechanical properties. (**D**) Summary of the tensile strengths and moduli of different hydrogel sheets. (**E**) Ashby diagram of tensile strength versus water content for concentric fibrous hydrogels compared with representative PVA hydrogels with enhanced mechanical properties in the literature. Literature data are summarized in table S2. (**F**) Capability of the tough concentric-RA hydrogel that could lift ~3000 times its own weight, demonstrating its potential as high-performance underwater materials with acoustic transparency. Scale bar, 50 mm. (**G**) Schematic of the experimental setup for (**H**) the measurement of ultrasound signals after traveling through Ecoflex and concentric-RA hydrogel samples with a thickness of 2 mm in a water medium. A source frequency of 2 MHz was used for the measurements. (**I**) Fatigue threshold of conc2sheet-RA hydrogels measured in longitudinal and circumferential directions. (**J**) Ashby diagram comparing the fatigue thresholds of conc2sheet-RA hydrogels with the reported fatigue-resistant isotropic hydrogels and anisotropic hydrogels. Literature data are summarized in table S3. Unless otherwise stated, all concentric-RA samples here were treated by 3 hours of rotary compression annealing. Data in [(B) and (D)] are means ± SD, $n = 3$ independent samples. Different letters above the bars in [(B) and (D)] indicate statistically significant differences between groups ($P < 0.05$), determined using one-way ANOVA with Tukey's test.

well as increases of 13-, 1.6-, 13-, and 24-fold in tensile modulus, stretchability, fracture strength and toughness, respectively, compared to the honey2sheet-RA$_=$ hydrogels (Fig. 5, C and D, and fig. S21C). By varying the rotary compression annealing time and polymer concentration, the tensile properties can be finely tuned (fig. S23), achieving tensile performance that is comparable to or even surpasses that of the top-performing tough hydrogels with high water content (Fig. 5E). It should be noted that, although the conc2sheet-RA has an interlaced circumferential fibrous structure, no delamination was observed along the radial direction of the hydrogel with a high cohesion force per unit width of 690 N/m (fig. S24). We demonstrate the potential of our concentric fibrous hydrogels as a high-performance underwater material with acoustic camouflaging properties (movie S4). The concentric fibrous hydrogels are mechanically tough, capable of lifting objects 3000 times heavier than themselves without permanent deformation while being highly acoustic transparent due to their high water content (Fig. 5F). The acoustic transmission of our concentric-RA hydrogel exceeds 95% at a source frequency of 2 MHz, far outperforming traditional flexible materials, such as Ecoflex, which reduced transmission by over 70% (Fig. 5, G and H).

Conventional hydrogels typically suffer from trade-offs between fracture toughness and modulus, as well as between fatigue threshold and modulus (*9*). Despite the improved tensile modulus, the fracture toughness of our conc2sheet-RA hydrogels can be simultaneously enhanced to ~80 kJ/m^2 (fig. S25), which is comparable to the reported top-performing isotropic PVA hydrogels (*17*). Moreover, our conc2sheet-RA hydrogels have superior isotropic fatigue resistance. Evaluated using a single-notch method, the conc2sheet-RA hydrogels exhibited fatigue thresholds of around 2320 J/m^2 in longitudinal and circumferential directions (Fig. 5I), surpassing existing isotropic fatigue-resistant hydrogels (Fig. 5J). Notably, this performance was achieved without using additive or salting-out agents. To further validate the exceptional fatigue resistance, we performed a cyclic fatigue test with a precut conc2sheet-RA hydrogel. No obvious crack propagation was observed after 30,000 cycles of stretching along an arbitrary direction at a high energy release rate of 2310 J/m^2 (fig. S26, B to D). Such mechanical improvement was attributed to their synergistic toughening mechanisms, including increased crystallinity, crack deflection, fibril pulling out, and fibril straightening at the crack tip contributed by the interlaced circumferential fibrous structures (fig. S27).

Ultracompressive properties

Many natural materials have concentric fibrous microstructures, providing them with extraordinary compressive properties. For instance, the annulus fibrosus of intervertebral discs, composed of concentric lamellae of collagen fibers, provides high stiffness to resist the pressure exerted by the nucleus pulposus during repetitive compression over a lifetime (*28*, *31*). Inspired by this, we examined the compressive properties of hydrogels with different structures. The results show that concentric-RA hydrogels outperformed honeycomb-RA and random-RA hydrogels in both axial and radial compressions (Fig. 6A). Notably, the compressive performance of concentric-RA hydrogels is particularly exceptional in the axial direction, with a compressive modulus of 0.96 MPa and a compressive stress of 10.7 MPa at 90% strain, which are more than 2.7 times higher than the performance of other hydrogels (Fig. 6B).

The effectiveness of the concentric fibrous structure in withstanding axial compression can be evident from the appearance of the compressed hydrogels. Honeycomb-A hydrogel experienced catastrophic cracking at its center under 90% axial strain, whereas concentric-A hydrogel was crack-free (fig. S29A). After rotary compression annealing, concentric-RA hydrogels demonstrated enhanced compressive properties (fig. S29B) and exceptional resilience with less than 6% permanent deformation at 85% axial compressive strain (Fig. 6C and movie S5). In contrast, honeycomb-RA and random-RA hydrogels suffered from notable permanent deformation. Furthermore, concentric-RA hydrogels demonstrate good compressive fatigue resistance. When subjected to a cyclic axial compressive strain of 60% after 500 cycles, concentric-RA hydrogel displayed the best strain recovery, with a residual strain of <11% immediately after compression and 8.3% after <1-hour recovery (Fig. 6, D and E, and fig. S29, C and D). In comparison, honeycomb-RA and random-RA hydrogels had residual strains over 30 and 20%, along with substantial reductions in maximum stress by 32 and 60%, respectively. Although not as superior as in the axial direction, concentric-RA hydrogels also demonstrated reduced residual strain compared to the honeycomb-RA and random-RA hydrogels during cyclic radial compression tests (fig. S30D).

To understand the ultracompressibility of the concentric hydrogels, we used finite element modeling to probe the fracture behaviors of concentric and honeycomb structures under axial and radial compressions (movie S6). Under axial compression, the honeycomb lattice buckles at mid-height, leading to localized stress and structural failure at ~30% strain (Fig. 6F). In contrast, the concentric structure can effectively distribute the stress, allowing it to withstand larger strain than the honeycomb structure. Similar findings were also observed in the simulation with a simple honeycomb unit and the simulations used representative volume elements (RVEs) to model the macroscopic mechanical behavior (fig. S31). It should be noted that our experimental results showed that the concentric-RA hydrogels can withstand a larger compressive strain than the simulated results. This discrepancy is probably because the interlaced structure in the concentric fibrous hydrogels was not considered in the simulations, and this structure can also effectively contribute to its compressibility (see Supplementary Text S3 for discussion). The simulation of radial compression behavior also aligns with the experimental data, revealing that the concentric model is capable of producing a greater radial compressive force and exhibiting a larger fracture strain than the honeycomb model (fig. S32B). The poorer radial compressibility of the honeycomb structure can be attributed to the weak connections between its longitudinally aligned fibers, which can be easily ruptured under radial compression (fig. S32C).

The extraordinary axial compressibility of concentric-RA hydrogels is further illustrated. Despite containing 85 wt % of water, a centimetric concentric-RA hydrogel can resist cutting by a sharp scalpel and can withstand a 65-kg human for over a minute without permanent failure (fig. S33, A and B). Impressively, a 1480-kg four-wheel car can repeatedly run over the concentric-RA hydrogel five times and remain on it for 10 s (Fig. 6G, fig. S33C, and movie S7). No fractures were observed, and its thickness retained over 86%. By contrast, the random-RA and honeycomb-RA hydrogels experienced over 25 and 43% permanent deformation after just one compression by the car. Noteworthy, the compressive stress of concentric-RA hydrogels surpasses that of the existing hydrogels produced with ice-templating

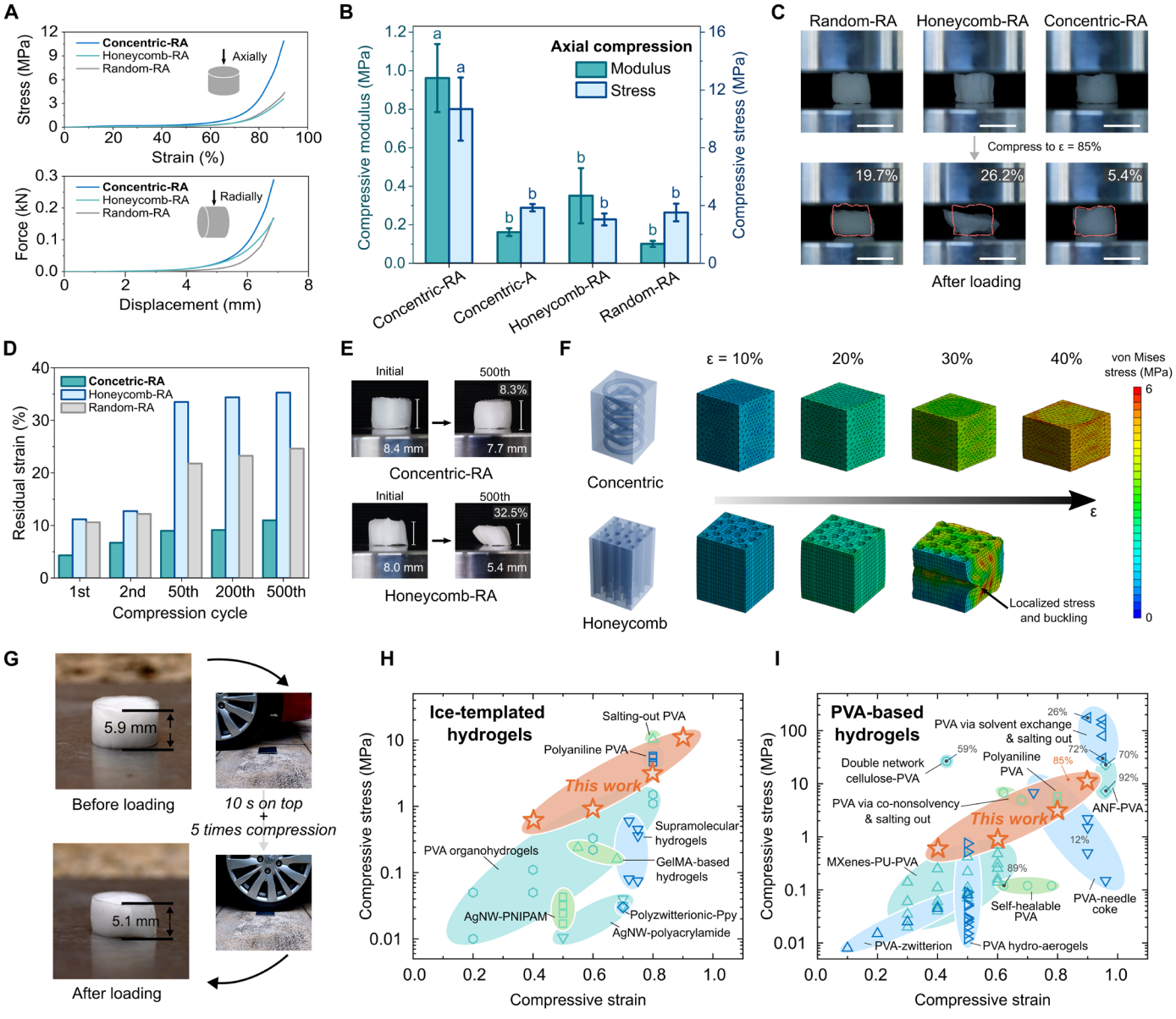

Fig. 6. Ultracompressive properties. (**A**) Stress-strain and force-displacement curves depicting the performance of hydrogels with different structures under axial and radial compression. (**B**) Summary of the axial compressive modulus and compressive stress at 90% strain for different hydrogels. (**C**) Photographs showing random-RA, honeycomb-RA, and concentric-RA after axial compression to a strain of 85%, with values at the upper right indicating the residual strains after compression. Scale bars, 10 mm. (**D**) Residual strains of different hydrogels over 500 cycles of axial compressive loading at 60% strain. (**E**) Photographs show the concentric-RA and honeycomb-RA hydrogels before compression and after <1-hour recovery following 500 axial compression cycles. The percentage values indicate the residual strains. (**F**) Simulated stress distributions in concentric and honeycomb structures under compressive loads. (**G**) Photographs of a concentric-RA hydrogel with a size of 5.9 mm (*L*) by 9.9 mm (*D*) before and after being compressed by a 1480-kg car for 10 s, followed by five consecutive compressions. (**H** and **I**) Ashby diagrams of compressive stress versus compressive strain for concentric-RA hydrogels compared with other reported hydrogels produced via ice-templating (H) and other reported PVA-based hydrogels with enhanced compressive mechanical properties (I). The percentage values indicate the water contents of the hydrogels reported in the literature, with some data omitted due to unavailability. Literature data are summarized in tables S4 and S5. Data in (B) are means ± SD, $n = 3$ independent samples. Different letters above the bars in (B) indicate statistically significant differences between groups ($P < 0.05$), determined using one-way ANOVA with Tukey's test. Unless otherwise stated, all -RA samples here were treated by 3 hours of rotary compression annealing.

methods and other top-performing PVA-based hydrogels with similar high water content reported in the literature (Fig. 6, H and I). This achievement is accomplished solely through structural design and crystallinity enhancement, without additives. The above results indicate the compelling potential of concentric fibrous hydrogels for load-bearing applications that require extreme compressive properties. Similar compressive properties can be achieved in samples of different diameters by simply adjusting the rotary compression annealing time to ensure complete densification of the polymeric scaffolds, which is ~50% reduction in diameter (fig. S34).

Burst pressure and hydrogel pneumatic actuators

Circumferentially aligned fibrous structures are often observed in pressure-withstanding biological organs in animals and marine creatures. For example, human arteries can endure pulsatile flow from ~3 billion cardiac cycles over a lifetime (*32*, *45*). This remarkable ability is partly attributed to their concentric lamellar layers and the circumferentially aligned collagen fibers in the tunica media, which evenly distribute stress and bear most stress generated by physiological pressure (*26*, *33*). In fish, swim bladders are internal gas-filled organs crucial for modulating buoyancy, allowing fish to stay at the desired water level. These organs consist of circumferentially oriented collagen fibers, which enable them to withstand high pressure (*29*, *30*). Inspired by their pressure-withstanding capabilities, we examined the pressure-resisting capacity of our concentric-RA hydrogels. Burst pressure tests were conducted. The concentric-RA hydrogels had a high burst pressure of 1.63 bar, which significantly exceeded that of honeycomb-RA (0.45 bar), random-RA (0.92 bar) hydrogels, and even Ecoflex (0.60 bar), a common material used in soft robotic applications (Fig. 7A).

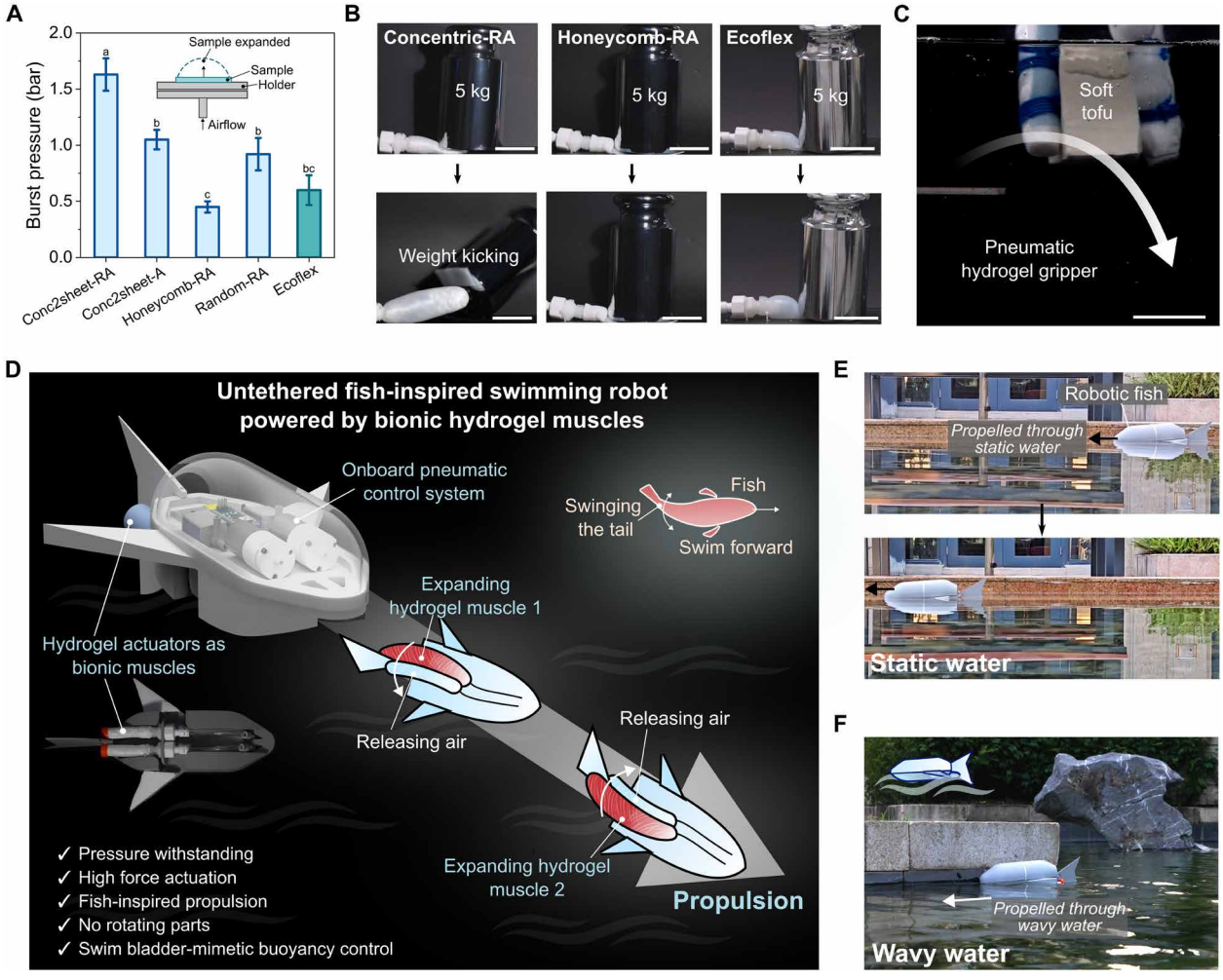

Fig. 7. High-pressure durability of concentric-RA pneumatic hydrogel actuators. (**A**) Burst pressure of different hydrogels and Ecoflex. The measurements were conducted with 3-mm-thick hydrogels. The inset shows the experimental setup, which is also illustrated in fig. S35. (**B**) Pneumatic hydrogel actuators made from concentric-RA hydrogels, honeycomb-RA hydrogels, and Ecoflex with a diameter of 25 mm and a length of 80 mm actuated at 0.45, 0.18, and 0.18 bar, respectively. The concentric-RA hydrogel actuator can generate sufficient actuation force to kick a 5-kg object due to its high pressurization capacity, whereas the honeycomb-RA and Ecoflex actuators failed to achieve this. Scale bars, 50 mm. (**C**) A hydrogel gripper composed of three concentric-RA chambers is capable of performing pick-and-place operations on soft and fragile objects. Scale bar, 30 mm. (**D**) Schematic illustrating the design and working principle of an untethered bioinspired robotic fish powered by alternating inflation and deflation of an antagonistic pair of concentric-RA actuators. (**E** and **F**) The untethered bioinspired fish robot can operate in static water (E) and wavy conditions (F) over long distances. Data in (A) are means ± SD, $n = 3$ independent samples. Different letters above the bars in (A) indicate statistically significant differences between groups ($P < 0.05$), determined using one-way ANOVA with Tukey's test.

The high burst pressure of our concentric fibrous hydrogels suggests their pressure-withstanding potential for pneumatic actuation applications. Whereas hydrogel actuators and robots offer advantages of skin-like touch, biocompatibility, and high water content (*46*), traditional hydrogel actuators often suffer from slow and low-force actuation (<1 N) (*47*, *48*). They are too soft and can swell, making stable pneumatic actuation difficult (*49*). We fabricated pneumatic actuators using concentric-RA, honeycomb-RA, and random-RA hydrogels (fig. S36A). The concentric-RA hydrogel actuators demonstrated a substantially higher pressurization capacity of 0.5 bar than the honeycomb-RA, random-RA, and Ecoflex actuators, which failed at 0.2, 0.25, and 0.2 bar, respectively (fig. S36B). This remarkable pressurized capability enables high actuation forces of the concentric-RA actuators. A small concentric-RA actuator can easily flip a 5-kg object, which is 800 times heavier than its hydrated weight, without bursting (Fig. 7B). Furthermore, the concentric-RA actuator showed fatigue resistance, capable of actuating continuously for more than 25,000 cycles over 14 hours (movie S8), attributed to their unique interlaced concentrically aligned fibrous structure that efficiently withstands circumferential stress. In contrast, other hydrogels have limited pressurization capacities due to their inappropriate microstructures (see Supplementary Text S4 for discussion). In particular, honeycomb hydrogels are prone to failure as the circumferential stress can easily crack through the unidirectional fibril direction. Besides, concentric-RA hydrogels show negligible swelling over 5 months, making them suitable for long-term applications (fig. S37). Compared to commonly used materials in soft actuators, such as Ecoflex, concentric-RA actuators offer advantages of higher pressurization capability, actuation with faster speed and higher force, tunable anisotropic deformability, and acoustic transparency while also providing tissue-like flexibility and high water content for biocompatibility (Fig. 5, G and H, and fig. S38).

By coupling multiple hydrogel pneumatic actuators, more complex tasks can be accomplished. A hydrogel gripper was created for the delicate manipulation of fragile items, such as ultrasoft tofu (Fig. 7C and movie S9). Furthermore, inspired by the swimming mechanism of natural fish (*50*), we designed an untethered robotic fish actuated by an antagonistic pair of hydrogel actuators (Fig. 7D). Figure S39 details our design with onboard processors, air pumps, sensors, and a power source. Natural fish swim by alternatively activating and contracting their right and left axial muscles to generate propulsive waves. In our case, the concentric-RA pneumatic hydrogel actuators are attached to the robotic fish tail, functioning as bionic muscles with high water content. These actuators are alternatively inflated and deflated by the onboard air pumps to create a swing motion for propulsion. The large pressurization capability of the hydrogel muscles allows the robot to generate sufficient propulsion force to navigate in both static and dynamic wavy water environments (Fig. 7, E and F, and movie S10). With a fully charged 2000-mA·hour battery, the untethered robotic fish can operate for more than 4 hours. Furthermore, the durability of the concentric-RA hydrogels enables long-term operation of the robotic fish, maintaining its functionality for at least 48 hours (~80,000 times actuation of the bionic muscles) (fig. S40A). This high pressurization capability also allows our concentric-RA hydrogel actuators to imitate the buoyancy-modulating functions of fish swim bladders. By varying the pressurization of the hydrogel chambers in a robotic fish, its buoyancy can be adjusted (fig. S40B). The above demonstrations showcase the potential of coupling the biomimetic pressure–withstanding concentric hydrogel actuators with swim bladder–mimetic buoyancy functions and fish-inspired propulsion for aquatic and underwater vehicles. This approach eliminates hard components and high-speed rotation to achieve propulsion and diving, ensuring gentle interaction with marine animals and thus minimizing harm to ecosystems.

DISCUSSION

This work presents a previously unknown ice-templating paradigm that creates circumferentially aligned fibrous structures in hydrogels. A freezing mechanism is proposed, revealing the importance of slow freezing in forming these structures. Enabled by the circumferentially aligned structure and a rotary compression annealing technique, the hydrogels demonstrate a record-breaking combination of tensile properties, fatigue resistance, ultracompressibility, and pressure durability, outperforming existing PVA hydrogels and ice-templated hydrogels with similar high water content. The interlaced concentrically aligned fibers in the hydrogels provide unique structural advantages in enhancing compressibility and pressure durability, which are challenging to achieve with the random and honeycomb structures produced using conventional freeze-thawing and ice-templating approaches (see Supplementary Text S3 and S4 for a detailed discussion on their structural advantages). These fibers can effectively withstand circumferential stress during pressurization, resist radial expansion during axial compression, and promote crack deflection. In addition, concentric ice-templating uses mild freezing temperatures (~−30°C) and avoids the need for costly cryogens, making it a more accessible alternative to conventional ice-templating approaches. The resulting properties enable high-performance applications in underwater environments and robotics. These include materials for underwater acoustic camouflage, pneumatic grippers for manipulating fragile objects, and high-force hydrogel actuators that function as bionic muscles of an untethered fish-inspired swimming robot and biomimetic swim bladders for buoyancy control, offering potential advantages for aquatic vehicles.

Considering the biomimetic structure-derived mechanical properties achieved with our hydrogels, future research could explore their potential in tissue engineering and bioengineering applications, such as artificial intervertebral discs and vascular grafts. These hydrogels can assist in replicating the biomechanical properties of native tissues while addressing mechanical mismatches associated with conventional implants. Furthermore, circumferentially aligned fibers can be harnessed to guide cell orientation in hydrogel biomaterials (e.g., silk) for the regeneration of circumferentially aligned tissue organizations, such as the alignment of muscle cells in biological vessels. It is also crucial to investigate the generalizability of the concentric ice-templating technique by examining factors that influence the growth of concentric ice structures in different hydrogels, including factors that affect the polymer-water interaction and the amount of free water in hydrogels (see Supplementary Text S2 for discussion). Overall, our work broadens the range of bioinspired structures achievable with ice-templating, highlighting the importance of structural designs in controlling mechanical properties.

MATERIALS AND METHODS

Experimental design

This study developed a previously unknown concentric freeze-casting technique to create hydrogels with bioinspired concentric structures. The effect of the freezing temperatures on the ice formation and ice growth in PVA solutions was investigated through in situ observation, revealing the underlying mechanism for the formation of these intricate concentric structures. The microstructures of the resulting freeze-casted scaffolds and hydrogels were characterized using confocal microscopy, SEM, and CT scan, allowing for a thorough analysis of their structural morphology, scalability, and consistency. Rotary compression annealing was designed and applied to the scaffolds to delicately preserve their microstructures while enhancing their crystallinity. Their crystalline structures were examined via SAXS and WAXS. Comprehensive tensile and compressive mechanical tests, as well as burst pressure tests, were conducted to assess their mechanical properties in comparison to traditional freeze-casted hydrogels. Finite element models were developed to elucidate the mechanisms behind their remarkable compressibility. The exceptional properties of these hydrogels, which surpass those of existing top-performing PVA hydrogels and freeze-casted hydrogels, were further demonstrated in car-compression tests, pneumatic grippers, and a bioinspired fish–inspired swimming robot.

Materials

All the chemicals in this study were used without further purification. PVA (molecular weight = 146~186 kDa, 99% hydrolyzed) and 5-([4,6-dichlorotriazin-2-yl]amino)fluorescein hydrochloride (5-DTAF) were purchased from Sigma-Aldrich. Glutaraldehyde solution (50 vol %) and hydrochloric acid (36.5 to 38 wt %) were obtained from Aladdin.

Preparation of PVA solutions

PVA solutions [2, 3, 5, and 7% (w/v)] were prepared by dissolving the PVA powder in deionized water at 100°C. The solutions were stirred in a container for at least 5 hours until a clear solution was obtained, and the container was loosely covered with its lid to prevent water evaporation. Afterward, the solutions were cooled down to room temperature before hydrogel fabrication.

Fabrication of the ice-templating molds

Cylindrical aluminum foil molds were used in the concentric ice-templating process. To prepare the molds, SolidWorks 2019 (Dassault Systemes) was used to design 3D models of cylindrical rods, which served as support for creating the molds. In this study, rods with a diameter ranging from 5 to 30 mm and a length between 50 and 200 mm were designed and 3D printed using a fused deposition modeling 3D printer (Ultimaker S3) with polylactic acid (PLA) materials. The printed rods were wrapped twice with aluminum foil (20 μm in thickness), which was then secured with aluminum tape, and its bottom was sealed with additional aluminum tape. Last, the rod support was removed to attain the cylindrical aluminum foil mold for subsequent fabrication procedures. These aluminum foil molds can be customized to create hydrogels in various dimensions.

To create polymeric scaffolds with honeycomb structures, molds used in a previous work on unidirectional freeze-casting were adopted (*15*). Specifically, molds with vertical slots, either in rectangular or cylindrical shapes, were designed and 3D printed with PLA.

Preparation of PVA hydrogels with concentric fibrous structures

Unless otherwise stated, a 5% (w/v) PVA solution was used to prepare the hydrogels. However, solution ranging from 2 to 7% (w/v) PVA was also used in this study. All solutions were degassed prior to the freezing process. Figure S1 outlines the procedure for fabricating concentric fibrous hydrogels. To create PVA hydrogels with concentric structures, PVA solution was poured into a cylindrical aluminum foil mold. The mold with the solution was then placed in a custom-built temperature-controlled freezing chamber or a standard freezer for slow freezing in an atmosphere at temperatures ranging from −20° to −40°C until the solution was fully frozen. Samples with sizes less than 30 mm (L) by 10 mm (D) were frozen for a minimum of 2 hours. Larger samples might require a longer freezing time. This process allows for the formation of concentrically templated ice in the PVA solution. The freezing rates at different temperatures were measured using type K thermocouples and a thermocouple data logger (TC-08, Pico Technology) (fig. S43). Unless otherwise stated, the freezing temperature used was −30°C.

After the freezing process, the samples were freeze-dried using a freeze dryer (10N/C, SCIENTZ) with a −80°C cold trap under a pressure of 1 Pa until all water was removed. The dried concentric fibrous polymeric scaffolds were then either annealed in an oven at 100°C for 90 min or annealed by rotary compression annealing. Figure S16A illustrates the custom-built setup designed for rotary compression annealing. In this method, the freeze-dried sample was placed between two heating pads, which were maintained at a temperature of 100°C. The upper heating pad was moved linearly at a speed of 15 mm/s by a gantry system to create a rotational motion to the samples, whereas an air cylinder (CU16-80, Chanto Air Hydraulics) installed between the gantry system and the upper pad applied increasing compression pressure at a rate of 0.5 bar/hour to the sample. This compression rate was chosen to optimize densification while preserving the circumferentially aligned structures (fig. S17). After annealing or rotary compression annealing, the polymeric scaffolds were reswelled in deionized water until equilibrium, resulting in the formation of concentric-A and concentric-RA hydrogels.

Tubular samples with concentric fibrous structures or conc-2sheet hydrogels were prepared using a similar method, with the addition of a rod placed at the center of the mold during freezing (fig. S21D). After freezing, the samples were freeze-dried. They were either treated with annealing in an oven at 100°C for 90 min or annealed by rotary compression annealing. The samples were then reswelled in deionized water. Conc2sheet hydrogels were prepared by cutting the tubular hydrogels into hydrogel sheets (fig. S21D). Unless otherwise stated, all concentric-RA and conc2sheet-RA samples were treated by 3 hours of rotary compression annealing.

Preparation of PVA hydrogels with other structures

PVA hydrogels with other structures were prepared for performance comparison. To create PVA hydrogels with a radial structure, a rapid freezing approach using a cylindrical mold was used. The cylindrical aluminum foil mold filled with PVA solution was placed either in a liquid nitrogen bath or in a custom-built freezing chamber set to a temperature ranging from −50° to −196°C for rapid freezing. For the preparation of PVA hydrogels with a honeycomb structure, the PVA solution was poured into the vertical slots of a PLA mold, which was placed on top of a copper block submerged in liquid nitrogen for unidirectional freeze-casting. To prepare PVA hydrogels with a random

porous structure, a PVA solution was frozen at −30°C for 8 hours, followed by thawing at room temperature for another 3 hours. This freeze-thaw process was repeated for a total of five cycles. The final samples were soaked in deionized water to equilibrium. All samples were then freeze-dried, treated with either annealing or rotary compression annealing, and reswelled in deionized water until equilibrium. The honey2sheet and ran2sheet hydrogels were fabricated using a similar method with a tubular mold as described in fig. S21D but used either unidirectional freeze-casting or a five-cycle freeze-thaw to attain the samples. The rotary compression annealing for the honeycomb-RA, random-RA, honey2sheet-RA, and ran2sheet-RA was conducted under the same condition used for the concentric-RA and conc2sheet-RA samples.

To prepare the chemically cross-linked PVA hydrogels, two aqueous solutions were first prepared: one containing 5 μl of glutaraldehyde (50 vol %, Aladdin) as a chemical cross-linker in 1 ml of 5% (w/v) PVA solution and the other with 5 μl of hydrochloric acid (36.5 to 38 wt %, Aladdin) as a cross-linking reaction accelerator in another 1 ml of 5% (w/v) PVA solution. The two PVA aqueous solutions were mixed using a centrifugal mixer (AR-100, Thinky), transferred into a mold, and cross-linked at room temperature for 3 hours. The cross-linked hydrogel sample was then soaked in deionized water for 2 days to remove unreacted chemicals.

In situ observation of ice growth

To observe the formation of ice crystals at various freezing temperatures, PVA aqueous solution was placed in a container with a size of 40 mm (L) by 40 mm (w) by 6 mm (H) and a wall thickness of 2 mm. An aluminum heat exchanger that was connected to a thermostatic chiller (DHJF-8005E, Greatwall) was placed next to one side of the container. The setup allowed for precise control of the cold surface temperature and established a directional temperature gradient within the solution. The formation of ice crystals in the solution was observed and recorded using a high-resolution camera with zoom functionality (EFL-LM-SM1000, EFL).

Microstructure characterizations

The microstructure of the polymeric scaffolds was examined using a field-emission scanning electron microscope (Merlin, Zeiss) at an acceleration voltage of 4 kV. All types of samples were analyzed by SEM before swelling in water in the fabrication procedure, except the freeze-thawed hydrogels, which were freeze-dried prior to SEM imaging. Before carrying out the SEM imaging, the samples were fractured using liquid nitrogen to expose either the perpendicular or transverse interface, and the fracture surfaces were then sputter coated with platinum using an ion sputtering device (Q150T ES, Quorum).

The μ-CT scan of the concentric fibrous polymeric scaffold was acquired using a μ-CT imaging system (Nano Voxel 2000, Sanying). The scanning parameters were set as follows: a spatial resolution of 4 μm, an x-ray tube voltage of 40 kV, an x-ray tube power of 10 kW, and a scanning step length of 4 μm. After scanning, the 3D volume of the sample was rendered using CTvox (version 3.3.1), and movie S1 with pseudocoloring was generated.

To observe the microstructures of the hydrated PVA hydrogel samples, hydrogels were reswelled in water until equilibrium. They were then frozen and cut into 50-μm-thick slices using a rotary microtome (NX70, Thermo Fisher Scientific). The slices were then chemically stained with a 5-DTAF fluorescent dye according to a previously reported protocol (*15*). The microstructure of the hydrogel slices was then imaged using a confocal laser scanning microscope (Stellaris 5, Leica). The directionality assessments of the SEM and confocal images were conducted using the OrientationJ plugin (Biomedical Image Group, EPFL, Switzerland) in ImageJ (version 1.54 g).

Measurement of water content

The water contents of the hydrogels (φ_{water}) were determined by measuring the weight difference between fully swollen and fully dried samples. Hydrogel samples were fully swollen in deionised water until equilibrium, and their weights were measured ($m_{swollen}$). After that, they were dried at 35°C for 12 hours and then at 90°C for 4 hours to ensure complete water removal. The weights of the dried sample were measured (m_{dry}), and the water contents were calculated using the following equation

$$\varphi_{water} = \left(m_{swollen} - m_{dry}\right) / m_{swollen} \times 100\,\% \quad (1)$$

Measurement of crystallinity

The crystallinities of the PVA hydrogels in their dry state were quantified using DSC (Themys One, Setaram). Following a previously reported protocol (*15*), the hydrogel samples were first chemically cross-linked with glutaraldehyde to fix the amorphous polymer chains, followed by air-drying in an oven at 37°C for 2 hours. The mass of the dried sample (with residual water) (m_{total}) was measured. The dried sample was then heated up at a rate of 10°C/min from 50° to 250°C with a nitrogen flow of 35 ml/min in the DSC machine. The resulting DSC curve reveals a broad peak between 60° and 160°C, which corresponds to the evaporation of residual water. Thus, the enthalpy for water evaporation per unit mass of the dried sample (with residual water) ($H_{residual}$) was determined by integrating the endothermic peak between 60° and 160°C. The mass of the residual water was calculated as $m_{residual} = m_{total} \times \left(H_{residual}/H^0_{water}\right)$, where $H^0_{water} = 2260\ \mathrm{J\ g^{-1}}$ is the latent heat for water evaporation. Another peak from 200° to 250°C in the DSC heating curve is associated with the melting of the PVA crystalline domains. The enthalpy for melting the crystalline domains per unit mass of the dried sample (with residual water) ($H_{crystalline}$) was estimated by integrating the endothermic peak from 200° to 250°C. Therefore, the mass of the crystalline domains ($m_{crystalline}$) was calculated as $m_{crystalline} = m_{total} \times \left(H_{crystalline}/H^0_{crystalline}\right)$, where $H^0_{crystalline} = 138.6\ \mathrm{J\ g^{-1}}$ is the enthalpy of fusion of 100% crystalline PVA. The crystallinity of the dried sample X (without residual water) was calculated as below

$$X = \left(m_{crystalline}\right) / \left(m_{total} - m_{water}\right) \times 100\% \quad (2)$$

X-ray scattering characterization

SAXS and WAXS tests were conducted on hydrogel samples at the BL10U1 and BL16B1 beamlines in the Shanghai Synchrotron Radiation Facility. The tests were performed using an x-ray radiation wavelength of 0.1239 nm. The sample-to-detector distances were set at 5245.19 mm (SAXS, BL10U1), 2201.86 mm (SAXS, BL16B1), and 205.53 mm (WAXS, BL10U1), and the exposure times were set at 1 s (BL10U1) and 15 s (BL16B1).

Fit2D software was used to analyze the 2D SAXS and WAXS patterns. The plots of the intensity (I) versus diffraction angle (2θ) obtained from WAXS patterns were used to determine the average sizes of crystalline domains (D), which were approximated using the Scherrer equation

$$D = k\lambda/(\beta\cos\theta) \quad (3)$$

where k is a dimensionless shape factor varying with the actual shape of the crystalline domain (set as 1, assuming a spherical shape of the crystalline domains), λ is the wavelength of x-ray diffraction, β is the half-width of the maximum diffraction, and θ is the Bragg angle. β and θ were identified from the I versus 2θ curves after subtracting the baseline.

The average intercrystal spacings (L) were determined from the Iq^2 versus q curves obtained from the SAXS patterns using the Bragg expression

$$L = 2\pi/q_{max} \quad (4)$$

where q_{max} is the q value at the peak intensity.

The Herman's orientation factors (f) were calculated using the below equations

$$f = \frac{3\langle\cos^2\varphi\rangle - 1}{2} \quad (5)$$

$$\langle\cos^2\varphi\rangle = \frac{\int_0^{\frac{\pi}{2}} I(\varphi)\sin\varphi\cos^2\varphi\,d\varphi}{\int_0^{\frac{\pi}{2}} I(\varphi)\sin\varphi\,d\varphi} \quad (6)$$

where φ is the azimuthal angle, and $I(\varphi)$ is the 1D SAXS scattering intensity as a function of φ.

Mechanical characterization

All mechanical tests, except for the fatigue threshold measurements, were performed at room temperature using a universal testing machine (C25.102, Shenzhen SANS) with a 500-N load cell. Tensile tests were conducted at a deformation rate of 50 mm/min. The cylindrical samples used in tensile tests, including the concentric-RA, honeycomb-RA, and random-RA, have a size of 25 mm (L) by 3 mm (D). All hydrogel sheet samples, including conc2sheet-RA, honey2sheet-RA, ran2sheet-RA, and conc2sheet-A, have a dimension of 25 mm (L) by 6 mm (w) by 2 mm (t). Before the tensile tests, they were cut from a fully swollen hydrogel sheet at random locations along the axis of interest. The selected locations did not affect the consistency of the mechanical results of the conc2sheet-RA samples (fig. S28). The stress (σ) was calculated as the measured force divided by the initial cross-sectional area of the sample. The strain (ε) was obtained as the ratio of the change in length to the initial length. The Young's moduli were the approximate linear fitting values of the stress-strain curves in the strain range of 5 to 10%. The tensile toughness was determined from the area under the stress-strain curves of unnotched samples until the fracture point.

To quantify fracture toughness, various groups of hydrogels with dimensions of 5 mm (L) by 24 mm (w) by 1 mm (t) were prepared, including both notched and unnotched samples. The notched samples were prepared by making a 4-mm-long precut at the middle of the sample using a razor blade. Both notched and unnotched samples of the same type were tested in tension at a strain rate of 20 mm/min to obtain one fracture toughness value. The notched sample was used to determine the critical strain (ε_c) at which crack propagation occurred. The fracture toughness, K, was then determined by integrating the area under the stress-strain (σ versus ε) curve of the unnotched sample from zero to ε_c and multiplying the area with the initial clamp distance (L_0) (Eq. 7)

$$K(\varepsilon_c) = L_0 \int_0^{\varepsilon_c} \sigma\,d\varepsilon \quad (7)$$

Fatigue threshold was determined using the single-notch method (*51*). All fatigue tests were performed using fully swollen hydrogel samples immersed in a water bath with a mechanical tester (CellScale, load cell = 44 N). Notched samples were prepared with a precut crack length of less than 1/5 of the sample width, specifically 0.5 mm, unless otherwise stated. Cyclic tensile tests were first conducted on the unnotched samples at a defined applied stretch (λ_A). The strain energy density of the unnotched sample, W, under the Nth cycle, when the loading-unloading curves become stable, was calculated using the following equation

$$W(\lambda_A, N) = \int_1^{\lambda_A} \sigma\,d\lambda \quad (8)$$

The same cyclic stretch of λ_A was then applied to the notched samples. The evolution of the crack length in the unloaded state (c) was recorded using a digital microscope (AM4815ZT, Dino-Lite).

The energy release rate (G) under the Nth cycle at λ_A was evaluated using Eq. 9

$$G(\lambda_A, N) = 2k(\lambda_A)\cdot c(N)\cdot W(\lambda_A, N) \quad (9)$$

k is a strain-dependent parameter, which was approximated as $k = 3\cdot\lambda_A^{-1/2}$ (*51*). By adjusting the applied stretch (λ_A), the relationship between the crack extension per cycle (dc/dN) and the corresponding energy release rate G was derived. By linearly extrapolating the curve of dc/dN versus G to the intercept with the abscissa, the fatigue threshold was identified. To validate the identified fatigue threshold, a notched hydrogel sample with a precrack length of ~0.5 mm was subjected to cyclic tensile loading at an energy release rate of 2310 J/m^2 for 30,000 cycles with crack propagation monitored using a camera.

Axial compression tests were carried out with cylindrical samples with a size of 10 mm (D) by 8 mm (L) at a compressive speed of 100 mm/min using a universal testing machine (C25.102, Shenzhen SANS), whereas radial compression tests used a sample size of 7.5 mm (D) by 5 mm (L). Cyclic compression tests were conducted at a deformation rate of 20 mm/min without waiting intervals. Unless otherwise stated, all the hydrogels used in the mechanical tests were prepared with a 5% (w/v) PVA solution. The samples subjected to rotary compression annealing (RA) were treated for 3 hours, whereas the samples subjected to standard annealing (A) were treated for 90 min. The car compression test was conducted with a 1480-kg four-wheel vehicle (Suzuki Swift).

Measurement of acoustic properties

Acoustic transmission properties of the concentric-RA and Ecoflex samples were measured in a water tank with ultrasonic transducers (LS-03A, YuZheng) using samples with dimensions of 40 mm (w) by 65 mm (L) by 2 mm (t). The sample was placed between two

transducers. A sinusoidal signal with a frequency of 2 MHz and a peak-to-peak voltage of 1.5 Vpp was generated by a signal generator (33210A, KEYSIGHT). The signal was boosted to 150 Vpp using a voltage amplifier (ATA7010, Aigtek) and was sent to a transducer as a signal source. During the measurement, the ultrasonic signal traveled through the sample, and the transmitted signal was measured by another transducer, which was connected to an oscillograph (UPO3202CS, UNI-T) with signal recording function as a receiver.

Burst pressure tests

Burst pressure tests were conducted using both hydrogel sheets and tubular hydrogels. For the tests with hydrogel sheets, a sample with a dimension of 30 mm (L) by 20 mm (w) by 3 mm (t) was fixed to a custom-made single-sided hermetic setup as shown in fig. S35. The setup was pressurized with incrementally increasing airflow, controlled by a pneumatic controller (OB1, Elveflow). The setup was increased by 50 mbar with each increment. In addition, the burst pressures of closed-end tubular hydrogel chambers were evaluated by directly applying air pressure to the hydrogels using the setup shown in fig. S36B. In all tests, the burst pressure was defined as the pressure when failure of the sample occurred.

Fabrication of a hydrogel gripper and an untethered fish robot

Prototypes of a hydrogel gripper and a bionic fish–inspired robot were created to demonstrate the pneumatic actuation capabilities of concentric hydrogels. To prepare the hydrogel gripper, three concentric-RA hydrogel chambers, which were treated with 0.5 hours of rotary compression annealing, were installed on a customized adapter connected to a pneumatic controller (OB1, Elveflow). Each hydrogel chamber was covered with cotton fabric on one side and wrapped with cotton yarn to enable bending motion and increase friction for gripping objects. An air pressure of 0.08 to 0.1 bar was used during operation for gripping, transporting, and releasing soft tofu.

For the preparation of the untethered bioinspired fish robot, customized parts, including the shell cover, the main body, and the tail, were designed in SolidWorks 2019 and were fabricated with PLA or polyethylene terephthalate glycol (PETG) filaments using a 3D printer (Ultimaker S3) (fig. S39A). Electrical components, including a battery, a microcontroller (Arduino NANO), small electric air pumps, miniature solenoid valves, and air pressure sensors (RSC-M171100k), were installed on a removable control box attached to the main body (fig. S39, B and C). Figure S39D shows the fabrication and the installation of the concentric-RA hydrogels actuators on the robotic fish. A pair of concentric-RA–3-hour hydrogel chambers, serving as bionic muscles, was produced via concentric ice-templating and was secured to the bottom surface of the main body and attached to the tail of the robot. The connection of the components and the control logic for the swimming operation are shown in fig. S39E. Specifically, each hydrogel chamber was connected to a valve, a pressure sensor, and an air pump. A controller was used to control the on/off operation of the air pump and the valve based on the pressure detection in each chamber. The swimming operation of the robot was achieved by alternately pressurizing to create wiggling motion of the fish tail.

Measurement of actuation speed

To evaluate the actuation speeds of chambers made from concentric-RA hydrogels and Ecoflex, videos of the actuations were captured using a high-speed camera (VEO-710S, AMETEK) at a sampling rate of 500 fps. The actuation pressure was controlled using a pneumatic controller (OB1, Elveflow). The actuation speeds in the axial and radial directions were determined by dividing the changes in the length and width of the chambers, resulting from the actuation, by the duration of the actuation.

Finite element modeling of compression behaviors

All mechanical simulations were carried out using the commercial software ANSYS 2024 (ANSYS 2024R1, ANSYS) to simulate the stress distribution within the hydrogels with honeycomb and concentric structures during compression loading. Five models were developed. They were the simple structural models of honeycomb and concentric geometries, a simple honeycomb unit model, as well as macroscopic models representing the two structures. All of these models were used to comprehensively study the axial compression behaviors of different structures, whereas the macroscopic models were used to simulate their radial compression behaviors. The geometries of the simple structural models can be found in fig. S31A. Each model has a size of 2 mm (w) by 2 mm (L) by 3 mm (t), and the diameter of the pores is 0.2 mm. The geometry of the simple honeycomb unit model is shown in fig. S31B. For the macroscopic models, the RVE method was used to develop the models. The dimensions of the RVE composites can be found in fig. S31C, which are a cube with a size of 330 μm by 330 μm by 330 μm, and the porosity of the RVE was kept at 0.1. The shape of the macroscopic model is set as a cylinder with a size of 5 mm (D) by 5 mm (h). The Material Designer module in ANSYS Workbench was used to compute the material parameters (Young's modulus, shear modulus, and Poisson's ratio) of the RVE orthotropic composite structures, including honeycomb and concentric structures. In all models, the matrix and pore-filling materials were assumed to be pure PVA and water, where the Young's modulus and Poisson's ratio of pure PVA were set as 0.5 MPa and 0.48, respectively. The linear elastic mechanism was used as a constitutive model to qualitatively reveal the mechanical response of materials during compressive loading. The maximum principal stress criterion was used to evaluate finite element failure, with the maximum fracture stress set at 0.06 MPa. Before analysis, an explicit meshing method was used to mesh the models using an auto minimum size setting. LS-DYNA (Lagrange) was used to simulate the compressive behaviors by setting the displacement as 50% of the sample's height. A friction coefficient of 0.1 was applied at the interface between the sample and the compression plate.

Statistical analysis

The quantitative experimental data are presented as means ± SD ($n = 3$ independent replicates). The statistical significance of datasets containing multiple groups was determined by one-way analysis of variance (ANOVA) with Tukey's test. A value of $P < 0.05$ was considered statistically significant.

Supplementary Materials

The PDF file includes:

Supplementary Text S1 to S6
Figs. S1 to S43
Tables S1 to S5
Legends for movies S1 to S10
References

Other Supplementary Material for this manuscript includes the following:
Movies S1 to S10

REFERENCES AND NOTES

1. U. G. K. Wegst, H. Bai, E. Saiz, A. P. Tomsia, R. O. Ritchie, Bioinspired structural materials. *Nat. Mater.* **14**, 23–36 (2015).
2. D. Nepal, S. Kang, K. M. Adstedt, K. Kanhaiya, M. R. Bockstaller, L. C. Brinson, M. J. Buehler, P. V. Coveney, K. Dayal, J. A. El-Awady, L. C. Henderson, D. L. Kaplan, S. Keten, N. A. Kotov, G. C. Schatz, S. Vignolini, F. Vollrath, Y. Wang, B. I. Yakobson, V. V. Tsukruk, H. Heinz, Hierarchically structured bioinspired nanocomposites. *Nat. Mater.* **22**, 18–35 (2023).
3. S. Ling, D. L. Kaplan, M. J. Buehler, Nanofibrils in nature and materials engineering. *Nat. Rev. Mater.* **3**, 18016 (2018).
4. J. Y. Sun, B. Bhushan, J. Tong, Structural coloration in nature. *RSC Adv.* **3**, 14862–14889 (2013).
5. M. Wu, Z. Y. Shao, N. Zhao, R. Zhang, G. Yuan, L. Tian, Z. Zhang, W. Gao, H. Bai, Biomimetic, knittable aerogel fiber for thermal insulation textile. *Science* **382**, 1379–1383 (2023).
6. A. R. Studart, Towards high-performance bioinspired composites. *Adv. Mater.* **24**, 5024–5044 (2012).
7. J.-Y. Sun, X. Zhao, W. R. K. Illeperuma, O. Chaudhuri, K. H. Oh, D. J. Mooney, J. J. Vlassak, Z. Suo, Highly stretchable and tough hydrogels. *Nature* **489**, 133–136 (2012).
8. X. Liu, J. Liu, S. Lin, X. Zhao, Hydrogel machines. *Mater. Today* **36**, 102–124 (2020).
9. X. Li, J. P. Gong, Design principles for strong and tough hydrogels. *Nat. Rev. Mater.* **9**, 380–398 (2024).
10. U. G. K. Wegst, P. H. Kamm, K. Yin, F. García-Moreno, Freeze casting. *Nat. Rev. Methods Primers* **4**, 28 (2024).
11. G. F. Shao, D. A. H. Hanaor, X. Shen, A. Gurlo, Freeze casting: From low-dimensional building blocks to aligned porous structures—A review of novel materials, methods, and applications. *Adv. Mater.* **32**, e1907176 (2020).
12. M. Hua, S. Wu, Y. Ma, Y. Zhao, Z. Chen, I. Frenkel, J. Strzalka, H. Zhou, X. Zhu, X. He, Strong tough hydrogels via the synergy of freeze-casting and salting out. *Nature* **590**, 594–599 (2021).
13. X. Guo, X. Dong, G. Zou, H. Gao, W. Zhai, Strong and tough fibrous hydrogels reinforced by multiscale hierarchical structures with multimechanisms. *Sci. Adv.* **9**, eadf7075 (2023).
14. X. Liang, G. Chen, S. Lin, J. Zhang, L. Wang, P. Zhang, Y. Lan, J. Liu, Bioinspired 2D isotropically fatigue-resistant hydrogels. *Adv. Mater.* **34**, e2107106 (2022).
15. X. Liang, G. Chen, S. Lin, J. Zhang, L. Wang, P. Zhang, Z. Y. Wang, Z. Wang, Y. Lan, Q. Ge, J. Liu, Anisotropically fatigue-resistant hydrogels. *Adv. Mater.* **33**, e2102011 (2021).
16. Z. Zhang, G. Chen, Y. Xue, Q. Duan, X. Liang, T. Lin, Z. Wu, Y. Tan, Q. Zhao, W. Zheng, L. Wang, F. Wang, X. Luo, J. Xu, J. Liu, B. Lu, Fatigue-resistant conducting polymer hydrogels as strain sensor for underwater robotics. *Adv. Funct. Mater.* **33**, 2305705 (2023).
17. X. Liang, G. Chen, I. M. Lei, P. Zhang, Z. Wang, X. Chen, M. Lu, J. Zhang, Z. Wang, T. Sun, Y. Lan, J. Liu, Impact-resistant hydrogels by harnessing 2D hierarchical structures. *Adv. Mater.* **35**, e2207587 (2023).
18. Y. Wang, H. Qin, Z. Li, J. Dai, H.-P. Cong, S.-H. Yu, Highly compressible and environmentally adaptive conductors with high-tortuosity interconnected cellular architecture. *Nat. Synth.* **1**, 975–986 (2022).
19. S. Miao, Y. Wang, L. Sun, Y. Zhao, Freeze-derived heterogeneous structural color films. *Nat. Commun.* **13**, 4044 (2022).
20. Y. Wei, H. Pan, J. Yang, C. Zeng, W. Wan, S. Chen, Aligned cryogel fibers incorporated 3D printed scaffold effectively facilitates bone regeneration by enhancing cell recruitment and function. *Sci. Adv.* **10**, eadk6722 (2024).
21. J.-W. Ma, F.-R. Zeng, X.-C. Lin, Y.-Q. Wang, Y.-H. Ma, X.-X. Jia, J.-C. Zhang, B.-W. Liu, Y.-Z. Wang, H.-B. Zhao, A photoluminescent hydrogen-bonded biomass aerogel for sustainable radiative cooling. *Science* **385**, 68–74 (2024).
22. H. Bai, Y. Chen, B. Delattre, A. P. Tomsia, R. O. Ritchie, Bioinspired large-scale aligned porous materials assembled with dual temperature gradients. *Sci. Adv.* **1**, e1500849 (2015).
23. N. Zhao, M. Li, H. Gong, H. Bai, Controlling ice formation on gradient wettability surface for high-performance bioinspired materials. *Sci. Adv.* **6**, eabb4712 (2020).
24. C. Wang, X. Chen, B. Wang, M. Huang, B. Wang, Y. Jiang, R. S. Ruoff, Freeze-casting produces a graphene oxide aerogel with a radial and centrosymmetric structure. *ACS Nano* **12**, 5816–5825 (2018).
25. S. E. Naleway, M. M. Porter, J. McKittrick, M. A. Meyers, Structural design elements in biological materials: Application to bioinspiration. *Adv. Mater.* **27**, 5455–5476 (2015).
26. X. Yu, R. Turcotte, F. Seta, Y. Zhang, Micromechanics of elastic lamellae: Unravelling the role of structural inhomogeneity in multi-scale arterial mechanics. *J. R. Soc. Interface* **15**, 20180492 (2018).
27. B. Chang, X. Liu, Osteon: Structure, turnover, and regeneration. *Tissue Eng. Part B Rev.* **28**, 261–278 (2022).
28. D. W. L. Hukins, J. R. Meakin, Relationship between structure and mechanical function of the tissues of the intervertebral joint. *Am. Zool.* **40**, 42–52 (2000).
29. J. L. Finney, G. N. Robertson, C. A. S. McGee, F. M. Smith, R. P. Croll, Structure and autonomic innervation of the swim bladder in the zebrafish (*Danio rerio*). *J. Comp. Neurol.* **495**, 587–606 (2006).
30. Z. Luan, S. Liu, W. Wang, K. Xu, S. Ye, R. Dan, H. Zhang, Z. Shu, T. Wang, C. Fan, M. Xing, S. Yang, Aligned nanofibrous collagen membranes from fish swim bladder as a tough and acid-resistant suture for pH-regulated stomach perforation and tendon rupture. *Biomater. Res.* **26**, 60 (2022).
31. N. D. Broom, A. Thambyah, Eds., "The intervertebral disc–endplate system" in *The Soft–Hard Tissue Junction: Structure, Mechanics and Function* (Cambridge Univ. Press, 2018), pp. 155–282.
32. L. E. Niklason, J. H. Lawson, Bioengineered human blood vessels. *Science* **370**, eaaw8682 (2020).
33. H. Wolinsky, S. Glagov, Structural basis for the static mechanical properties of the aortic media. *Circ. Res.* **14**, 400–413 (1964).
34. S. Ladet, L. David, A. Domard, Multi-membrane hydrogels. *Nature* **452**, 76–79 (2008).
35. B. C. Zarket, S. R. Raghavan, Onion-like multilayered polymer capsules synthesized by a bioinspired inside-out technique. *Nat. Commun.* **8**, 193 (2017).
36. T. A. Ogden, M. Prisbrey, I. Nelson, B. Raeymaekers, S. E. Naleway, Ultrasound freeze casting: Fabricating bioinspired porous scaffolds through combining freeze casting and ultrasound directed self-assembly. *Mater. Des.* **164**, 107561 (2019).
37. K. Yin, P. Divakar, U. G. K. Wegst, Freeze-casting porous chitosan ureteral stents for improved drainage. *Acta Biomater.* **84**, 231–241 (2019).
38. L. Fan, J.-L. Li, Z. Cai, X. Wang, Creating biomimetic anisotropic architectures with co-aligned nanofibers and macrochannels by manipulating ice crystallization. *ACS Nano* **12**, 5780–5790 (2018).
39. S. R. Stauffer, N. A. Peppast, Poly(vinyl alcohol) hydrogels prepared by freezing-thawing cyclic processing. *Polymer* **33**, 3932–3936 (1992).
40. S. Lin, J. Liu, X. Liu, X. Zhao, Muscle-like fatigue-resistant hydrogels by mechanical training. *Proc. Natl. Acad. Sci. U.S.A.* **116**, 10244–10249 (2019).
41. Y. Bi, B. Cao, T. Li, Enhanced heterogeneous ice nucleation by special surface geometry. *Nat. Commun.* **8**, 15372 (2017).
42. K.-Y. Chan, X. Shen, J. Yang, K.-T. Lin, H. Venkatesan, E. Kim, H. Zhang, J.-H. Lee, J. Yu, J. Yang, J.-K. Kim, Scalable anisotropic cooling aerogels by additive freeze-casting. *Nat. Commun.* **13**, 5553 (2022).
43. R. Ricciardi, F. Auriemma, C. De Rosa, F. Lauprêtre, X-ray diffraction analysis of poly(vinyl alcohol) hydrogels, obtained by freezing and thawing techniques. *Macromolecules* **37**, 1921–1927 (2004).
44. X. Zhang, H. Yan, C. Xu, X. Dong, Y. Wang, A. Fu, H. Li, J. Y. Lee, S. Zhang, J. Ni, M. Gao, J. Wang, J. Yu, S. S. Ge, M. L. Jin, L. Wang, Y. Xia, Skin-like cryogel electronics from suppressed-freezing tuned polymer amorphization. *Nat. Commun.* **14**, 5010 (2023).
45. M. S. Sacks, A. P. Yoganathan, Heart valve function: A biomechanical perspective. *Philos. Trans. R. Soc. London Ser. B Biol. Sci.* **362**, 1369–1391 (2007).
46. Y. S. Zhang, A. Khademhosseini, Advances in engineering hydrogels. *Science* **356**, eaaf3627 (2017).
47. M. Li, X. Wang, B. Dong, M. Sitti, In-air fast response and high speed jumping and rolling of a light-driven hydrogel actuator. *Nat. Commun.* **11**, 3988 (2020).
48. H. Na, Y.-W. Kang, C. S. Park, S. Jung, H.-Y. Kim, J.-Y. Sun, Hydrogel-based strong and fast actuators by electroosmotic turgor pressure. *Science* **376**, 301–307 (2022).
49. H. Yuk, S. Lin, C. Ma, M. Takaffoli, N. X. Fang, X. Zhao, Hydraulic hydrogel actuators and robots optically and sonically camouflaged in water. *Nat. Commun.* **8**, 14230 (2017).
50. C. Wardle, J. Videler, J. Altringham, Tuning in to fish swimming waves: Body form, swimming mode and muscle function. *J. Exp. Biol.* **198**, 1629–1636 (1995).
51. S. Lin, X. Liu, J. Liu, H. Yuk, H.-C. Loh, G. A. Parada, C. Settens, J. Song, A. Masic, G. H. McKinley, X. H. Zhao, Anti-fatigue-fracture hydrogels. *Sci. Adv.* **5**, eaau8528 (2019).
52. S. Wu, Z. He, J. Zang, S. Jin, Z. Wang, J. Wang, Y. Yao, J. Wang, Heterogeneous ice nucleation correlates with bulk-like interfacial water. *Sci. Adv.* **5**, eaat9825 (2019).
53. H. Yuk, T. Zhang, S. Lin, G. A. Parada, X. Zhao, Tough bonding of hydrogels to diverse non-porous surfaces. *Nat. Mater.* **15**, 190–196 (2016).
54. L. Xu, X. Zhao, C. Xu, N. A. Kotov, Water-rich biomimetic composites with abiotic self-organizing nanofiber network. *Adv. Mater.* **30**, 1703343 (2018).
55. L. Xu, Y. Qiao, D. Qiu, Coordinatively stiffen and toughen hydrogels with adaptable crystal-domain cross-linking. *Adv. Mater.* **35**, e2209913 (2023).
56. M. Sun, H. Li, Y. Hou, N. Huang, X. Xia, H. Zhu, Q. Xu, Y. Lin, L. Xu, Multifunctional tendon-mimetic hydrogels. *Sci. Adv.* **9**, eade6973 (2023).
57. T. Li, H. Qi, Y. Zhao, P. Kumar, C. Zhao, Z. Li, X. Dong, X. Guo, M. Zhao, X. Li, X. Wang, R. O. Ritchie, W. Zhai, Robust and sensitive conductive nanocomposite hydrogel with bridge cross-linking-dominated hierarchical structural design. *Sci. Adv.* **10**, eadk6643 (2024).
58. H. He, H. Li, A. Pu, W. Li, K. Ban, L. Xu, Hybrid assembly of polymeric nanofiber network for robust and electronically conductive hydrogels. *Nat. Commun.* **14**, 759 (2023).
59. S. Huang, X. Liu, S. Lin, C. Glynn, K. Felix, A. Sahasrabudhe, C. Maley, J. Xu, W. Chen, E. Hong, A. J. Crosby, Q. Wang, S. Rao, Control of polymers' amorphous-crystalline

transition enables miniaturization and multifunctional integration for hydrogel bioelectronics. *Nat. Commun.* **15**, 3525 (2024).
60. S. Zhu, S. Wang, Y. Huang, Q. Tang, T. Fu, R. Su, C. Fan, S. Xia, P. S. Lee, Y. Lin, Bioinspired structural hydrogels with highly ordered hierarchical orientations by flow-induced alignment of nanofibrils. *Nat. Commun.* **15**, 118 (2024).
61. Y. Wu, Y. Zhang, H. Wu, J. Wen, S. Zhang, W. Xing, H. Zhang, H. Xue, J. Gao, Y. Mai, Solvent-exchange-assisted wet annealing: A new strategy for superstrong, tough, stretchable, and anti-fatigue hydrogels. *Adv. Mater.* **35**, e2210624 (2023).
62. R. Bai, Q. Yang, J. Tang, X. P. Morelle, J. Vlassak, Z. Suo, Fatigue fracture of tough hydrogels. *Extreme Mech. Lett.* **15**, 91–96 (2017).
63. H. Lei, L. Dong, Y. Li, J. Zhang, H. Chen, J. Wu, Y. Zhang, Q. Fan, B. Xue, M. Qin, B. Chen, Y. Cao, W. Wang, Stretchable hydrogels with low hysteresis and anti-fatigue fracture based on polyprotein cross-linkers. *Nat. Commun.* **11**, 4032 (2020).
64. W. Zhang, X. Liu, J. Wang, J. Tang, J. Hu, T. Lu, Z. Suo, Fatigue of double-network hydrogels. *Eng. Fract. Mech.* **187**, 74–93 (2018).
65. X. Li, K. Cui, T. L. Sun, L. Meng, C. Yu, L. Li, C. Creton, T. Kurokawa, J. P. Gong, Mesoscale bicontinuous networks in self-healing hydrogels delay fatigue fracture. *Proc. Natl. Acad. Sci. U.S.A.* **117**, 7606–7612 (2020).
66. B. Xue, Z. Bashir, Y. Guo, W. Yu, W. Sun, Y. Li, Y. Zhang, M. Qin, W. Wang, Y. Cao, Strong, tough, rapid-recovery, and fatigue-resistant hydrogels made of picot peptide fibres. *Nat. Commun.* **14**, 2583 (2023).
67. J. Wang, Y. Song, F. Yu, Y. Zeng, C. Wu, X. Qin, L. Peng, Y. Li, Y. Zhou, R. Tao, H. Liu, H. Zhu, M. Sun, W. Xu, C. Zhang, Z. Wang, Ultrastrong, flexible thermogalvanic armor with a Carnot-relative efficiency over 8%. *Nat. Commun.* **15**, 6704 (2024).
68. L. Li, Y. Zhang, H. Lu, Y. Wang, J. Xu, J. Zhu, C. Zhang, T. Liu, Cryopolymerization enables anisotropic polyaniline hybrid hydrogels with superelasticity and highly deformation-tolerant electrochemical energy storage. *Nat. Commun.* **11**, 62 (2020).
69. X. Dong, X. Guo, Q. Liu, Y. Zhao, H. Qi, W. Zhai, Strong and tough conductive organo-hydrogels via freeze-casting assisted solution substitution. *Adv. Funct. Mater.* **32**, 2203610 (2022).
70. Z. Luo, G. Tang, H. Ravanbakhsh, W. Li, M. Wang, X. Kuang, C. E. Garciamendez-Mijares, L. Lian, S. Yi, J. Liao, M. Xie, J. Guo, Z. Zhou, Y. S. Zhang, Vertical extrusion cryo(bio)printing for anisotropic tissue manufacturing. *Adv. Mater.* **34**, e2108931 (2022).
71. Z. Ye, T. Chi, C. J. Evans, D. Liu, C. J. Addonizio, B. Su, I. Pramudya, Y. Xiang, R. K. Roeder, M. J. Webber, Implications of supramolecular crosslinking on hydrogel toughening by directional freeze-casting and salting-out. *Adv. Funct. Mater.* **34**, 2402613 (2024).
72. C. Lei, J. Park, W. Guan, Y. Zhao, K. P. Johnston, G. Yu, Biomimetically assembled sponge-like hydrogels for efficient solar water purification. *Adv. Funct. Mater.* **33**, 2303883 (2023).
73. P. Song, H. Qin, H.-L. Gao, H.-P. Cong, S.-H. Yu, Self-healing and superstretchable conductors from hierarchical nanowire assemblies. *Nat. Commun.* **9**, 2786 (2018).
74. H. Liu, C. Du, L. Liao, H. Zhang, H. Zhou, W. Zhou, T. Ren, Z. Sun, Y. Lu, Z. Nie, F. Xu, J. Zhu, W. Huang, Approaching intrinsic dynamics of MXenes hybrid hydrogel for 3D printed multimodal intelligent devices with ultrahigh superelasticity and temperature sensitivity. *Nat. Commun.* **13**, 3420 (2022).
75. Z. Wang, N. Li, X. Yang, Z. Zhang, H. Zhang, X. Cui, Thermogalvanic hydrogel-based e-skin for self-powered on-body dual-modal temperature and strain sensing. *Microsyst. Nanoeng.* **10**, 55 (2024).
76. Z. Wang, X. Xu, Y. Xu, W. Lin, Z. Peng, A ternary heterogeneous hydrogel with strength elements for resilient, self-healing, and recyclable epidermal electronics. *NPJ Flex. Electron.* **6**, 51 (2022).
77. H. Zhou, X. Wei, A. Liu, S. Wang, B. Chen, Z. Chen, M. Lyu, W. Guo, X. Cao, M. Ye, Tough hydro-aerogels with cation specificity enabled ultra-high stability for multifunctional sensing and quasi-solid-state electrolyte applications. *Adv. Mater.* **36**, e2313088 (2024).
78. Y. Yan, S. Duan, B. Liu, S. Wu, Y. Alsaid, B. Yao, S. Nandi, Y. Du, T.-W. Wang, Y. Li, X. He, Tough hydrogel electrolytes for anti-freezing zinc-ion batteries. *Adv. Mater.* **35**, e2211673 (2023).
79. H. Zou, X. Meng, X. Zhao, J. Qiu, Hofmeister effect-enhanced hydration chemistry of hydrogel for high-efficiency solar-driven interfacial desalination. *Adv. Mater.* **35**, e2207262 (2023).
80. F. Yang, J. Zhao, W. J. Koshut, J. Watt, J. C. Riboh, K. Gall, B. J. Wiley, A synthetic hydrogel composite with the mechanical behavior and durability of cartilage. *Adv. Funct. Mater.* **30**, 2003451 (2020).

Acknowledgments: We would like to thank I. Wong and Q. Liu for help with the DSC measurements; D. Fang, Z. Liao, and F. Liu for help with the microstructure characterization; J. Feng, Z. Gao, L. Wong, and Z. Wang for support with the SAXS and WAXS measurements; B. Wang, Y. Guo, and P. Tan for assisting with the experiments; and W. Wang for the insightful discussion. **Funding:** I.M.L. acknowledges the financial support by the Science and Technology Development Fund, Macau SAR (0119/2022/A3, 0009/2023/ITP1, and 0113/2024/RIB2), and the Research Grant from the University of Macau and the University of Macau Development Foundation (SRG2022-00038-FST and MYRG-GRG2023-00225-FST-UMDF). **Author contributions:** Conceptualization: W.G., S.Y., X.L., and I.M.L. Methodology: W.G., S.Y., Y.Z., P.N., X.L., C.W., J.L., and I.M.L. Investigation: W.G., S.Y., D.Z., Y.Z., C.C., C.T.K., B.Z., Y.Y.S.H., J.L., and I.M.L. Data curation: W.G., S.Y., P.N., J.L., and I.M.L. Validation: W.G., S.Y., Y.Z., P.N., and I.M.L. Formal analysis: W.G., S.Y., Y.Y.S.H., and I.M.L. Software: W.G., S.Y., and P.N. Visualization: W.G., S.Y., and I.M.L. Resources: C.T.K., C.W., Y.Y.S.H., J.L., and I.M.L. Supervision: Y.Y.S.H. and I.M.L. Project administration: I.M.L. Funding acquisition: I.M.L. Writing—original draft: W.G., S.Y., P.N., X.L., and I.M.L. Writing—review and editing: W.G., S.Y., D.Z., X.L., C.T.K., B.Z., C.W., J.L., and I.M.L. **Competing interests:** I.M.L. and W.G. are inventors on one pending patent application related to this work filed by the University of Macau with the China National Intellectual Property Administration (application no. 2025100281272, filed on 8 January 2025). The other authors declare that they have no competing interests. **Data and materials availability:** All data needed to evaluate the conclusions in the paper are present in the paper and/or the Supplementary Materials.

Submitted 7 January 2025
Accepted 16 May 2025
Published 20 June 2025
10.1126/sciadv.adv7786